Materials & Design 212 (2021) 110212

Contents lists available at ScienceDirect

Materials & Design

journal homepage: www.elsevier.com/locate/matdes

Continuum micromechanics model for fired clay bricks: Upscaling of experimentally identified microstructural features to macroscopic elastic stiffness and thermal conductivity

Thomas Buchner [a,*], Thomas Kiefer [a], Markus Königsberger [a,b], Andreas Jäger [c], Josef Füssl [a]

[a] Institute for Mechanics of Materials and Structures, TU Wien, Karlsplatz 13/202, 1040 Vienna, Austria
[b] BATir Department, Université libre de Bruxelles, CP194/04, 50 avenue F.D. Roosevelt, Brussels 1050, Belgium
[c] Wienerberger AG, Wienerbergerplatz 1, 1100 Vienna, Austria

HIGHLIGHTS

- Unique multiscale representation to model the microstructure of different clay bricks.
- Model-predicted elastic stiffness and thermal conductivity match experimental results.
- Neither stiffness nor conductivity are generally correlated to the brick density.
- The developed model paves the way for efficient optimization of modern brick products.

GRAPHICAL ABSTRACT

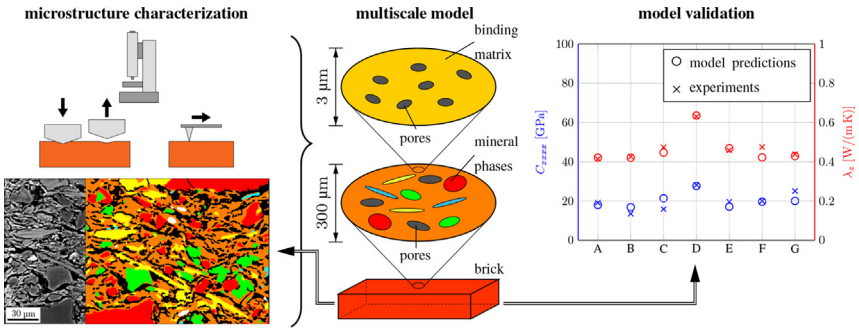

ARTICLE INFO

Article history:
Received 30 June 2021
Revised 5 October 2021
Accepted 31 October 2021
Available online 2 November 2021

Keywords:
Clay brick
Multiscale model
Elastic stiffness
Thermal conductivity

ABSTRACT

Quantification of elastic stiffness and thermal conductivity of fired clay bricks is still often limited to empirical rules and laboratory testing, which becomes progressively more challenging given the large variety of raw materials used to optimize the properties of modern brick products. Applying a continuum micromechanics multiscale approach, we herein aim at upscaling of microstructural features to quantify the bricks' macroscopic properties. Microstructural features such as assemblage and morphometry of mineral phases (quartz, feldspar, and micas), of pores, and of the binding matrix phase, respectively, as well as thermoelastic phase properties are provided by recently published results from extensive microscopic testing including electron microscopy imaging, mercury intrusion porosimetry, nanoindentation, and scanning thermal microscopy. These results are incorporated into the micromechanics model by introducing spheroidal phases with characteristic orientation distribution at two observation scales. The homogenized macroscopic stiffness and conductivity agree very well with independent results from novel macroscopic tests for all seven studied brick compositions. This corroborates the microstructure-informed multiscale model approach and its assumptions: the linear increase of the binding matrix properties with the material's carbonate content, and the inability of large quartz with interface cracks to take over any mechanical loads.

1. Introduction

Fired clay bricks, a building material which requires both sufficient mechanical performance and thermal insulation, are pro-

* Corresponding author.
E-mail address: thomas.buchner@tuwien.ac.at (T. Buchner).

https://doi.org/10.1016/j.matdes.2021.110212
0264-1275/

duced from various mixtures of clayey raw materials, potentially blended with pore forming additives or tempers, extruded, dried, and fired subsequently. The macroscopic strength, stiffness, and thermal conductivity of bricks – and thus also of masonry [11,37,61] – are tied closely to the brick microstructure [48,49,30,18,25,26] which, in turn, is a result of the raw clay composition and the brick processing. The brick microstructure is composed of nano- to micrometer-sized pores and crystalline mineral grains, the latter are "glued together" by a glassy matrix-like constituent resulting from fusing of the clays during firing. Geometrical features of this microstructure have been characterized extensively, using scanning electron microscopy (SEM), mercury intrusion porosimetry (MIP), and micro-computed tomography (μ-CT) [43,15,16,1,34,36,10,9]. Mechanical and thermal properties of the microstructural constituents, in turn, were quantified by means of nanoindentation [43,35] and scanning thermal microscopy [38]. Despite the aforementioned considerable progress in microstructure characterization in recent years, links of microstructure and mineralogy to macroscopic mechanical and thermal brick properties are often only of qualitative nature [18,30,12] or based on phenomenological models [25,26,29]. Microstructure-based models, either analytical approaches [57,53–55,72,71] or numerical finite element approaches [28,64,33], in turn, are often limited to quantifying the effect of the porosity.

We herein aim at taking advantage of the experimentally derived quantitative microstructural data and at translating them to mechanical and thermal macroscopic brick properties. For bridging the micro-to-macro gap, we use a continuum micromechanics approach [68], motivated by successful, physics-based predictions of macroscopic properties of several heterogeneous building materials including concrete [56,8,42,45], wood [4,24], bituminous mixtures [20,67,69], and very recently also fired clay bricks [38]. These models resolve the material's microstructure at distinct observation scales. At each observation scale, experimentally quantified features of the different microstructural constituents, such as morphometrical properties, are represented adequately by means of introducing spheroidal material phases with characteristic aspect ratios, volume fractions, and orientation distributions. While these morphological properties might depend on the actual material composition, the mechanical or thermal properties of distinct constituents are typically intrinsic, i.e. they do not change from one composition to another. The macroscopic material properties, for a wide range of material compositions, are predicted by applying homogenization theory [32,6,68].

As for fired clay bricks, Kiefer et al. [38] developed such a micromechanics multiscale approach to predict the macroscopic thermal conductivity. To model the complex microstructure, the authors distinguished an anisotropic glassy matrix phase, anisotropic mineral phases (e.g. quartz and feldspar), and pore phases. Minerals and pores are modeled as oblate spheroids with preferred orientation along the extrusion plane. Homogenization of thermal conductivities for media with oriented ellipsoidal inclusions is performed based on the theoretical developments of Giraud et al. [27]. In the present work, we aim at extending the aforementioned model in two directions, (i) through consideration of seven mineralogically very different fired clay bricks, representing a wide range of clayey raw materials used in the European brick industry, and (ii) through homogenization of the macroscopic elastic stiffness together with the macroscopic thermal conductivity. Regarding the different compositions, access to morphometric phase properties, phase stiffness and phase conductivity is provided by recently published data from extensive laboratory testing at different length scales [34–36,38,10,9]. Regarding stiffness homogenization, particular focus is given to the role of quartz grains which often exhibit cracks at or close to their surface. In order to carefully validate the model, macroscopic experiments including ultrasound testing and heat flow measurements are conducted for all seven brick compositions.

2. Multiscale micromechanics material model

2.1. Materials and modeling strategy

The study focuses on extruded clay bricks fired at 880 °C produced from seven different clays, which are widely used in the European brick industry. They are herein labeled as clays A-G[1], and originate from Somogy county in Hungary (clay A), Olomouc region in Czech Republic (B and D), state of Brandenburg in Germany (C), Szabolcs-Szatmár-Bereg county in Hungary (E), state of Lower Austria in Austria (F), and Karlovac county in Croatia (G). The fired clay bricks are macroscopically homogeneous but exhibit a complex hierarchically organized microstructure, whereby heterogeneities can be resolved at different observation scales, as shown in Fig. 1. Microstructural features depend on the composition: brick A shows a very fine-grained structure, bricks B, E, and F exhibit uniformly distributed larger grains, while bricks C and G contain very large quartz grains embedded in a dense matrix material, see the comprehensive microstructure investigations of Kariem et al. [34–36] and Buchner et al. [10,9] for more details. Despite these differences, the basic microstructural fingerprint – consisting of mineral grains, and pores, orientated preferably in extrusion direction (x-direction in Fig. 1) – is similar in all bricks. This way, we aim at modeling the microstructure with a unique representation valid for any clay composition, but with composition-dependent assemblage and morphometry of microstructural constituents.

A micromechanics multiscale model for fired clay bricks, recently developed by Kiefer et al. [38], is therefore applied and extended for the prediction of the macroscopic elastic stiffness and the macroscopic thermal conductivity. Thereby, transverse isotropy is assumed, which has been shown in previous studies to suitably describe the generally orthotropic macroscopic behavior of extruded bricks [38,43,5]. The model rests on two sets of experiments performed by our research group, as depicted in the flowchart in Fig. 2. On the one hand, geometrical information on microstructural constituents, i.e. amounts and morphometric quantities are obtained from published data from scanning electron microscopy (SEM) coupled with Energy-dispersive X-ray spectroscopy (EDX), from powder X-ray diffraction (PXRD), from X-ray fluorescence spectroscopy (XRF), from computed tomography scanning (μ-CT), and from mercury intrusion porosimetry (MIP), see Kariem et al. [34,36] and Buchner et al. [10,9]. Access to the universal mechanical and thermal properties of the constituents, on the other hand, is provided by means of published data from nanoindentation [35] and from atomic force microscope-based scanning thermal microscopy (AFM-SThM) [38]. Model-predicted elastic stiffnesses and thermal conductivities for bricks made from seven different clay mixtures are then compared to novel experimental data obtained from ultrasound and heat flow testing, see Section 3.

2.2. Micromechanical representation

Fired clay brick is modeled by means of a continuum micromechanics approach. In continuum micromechanics, a material is understood as a macro-homogeneous, but micro-heterogeneous body, which is resolved by means of one or many representative

[1] The labels A-E are also used in Buchner et al. [10], the materials labeled with G and F were denoted as HD 880 and KV 880, respectively, in Kariem et al. [34] and Kiefer et al. [38].

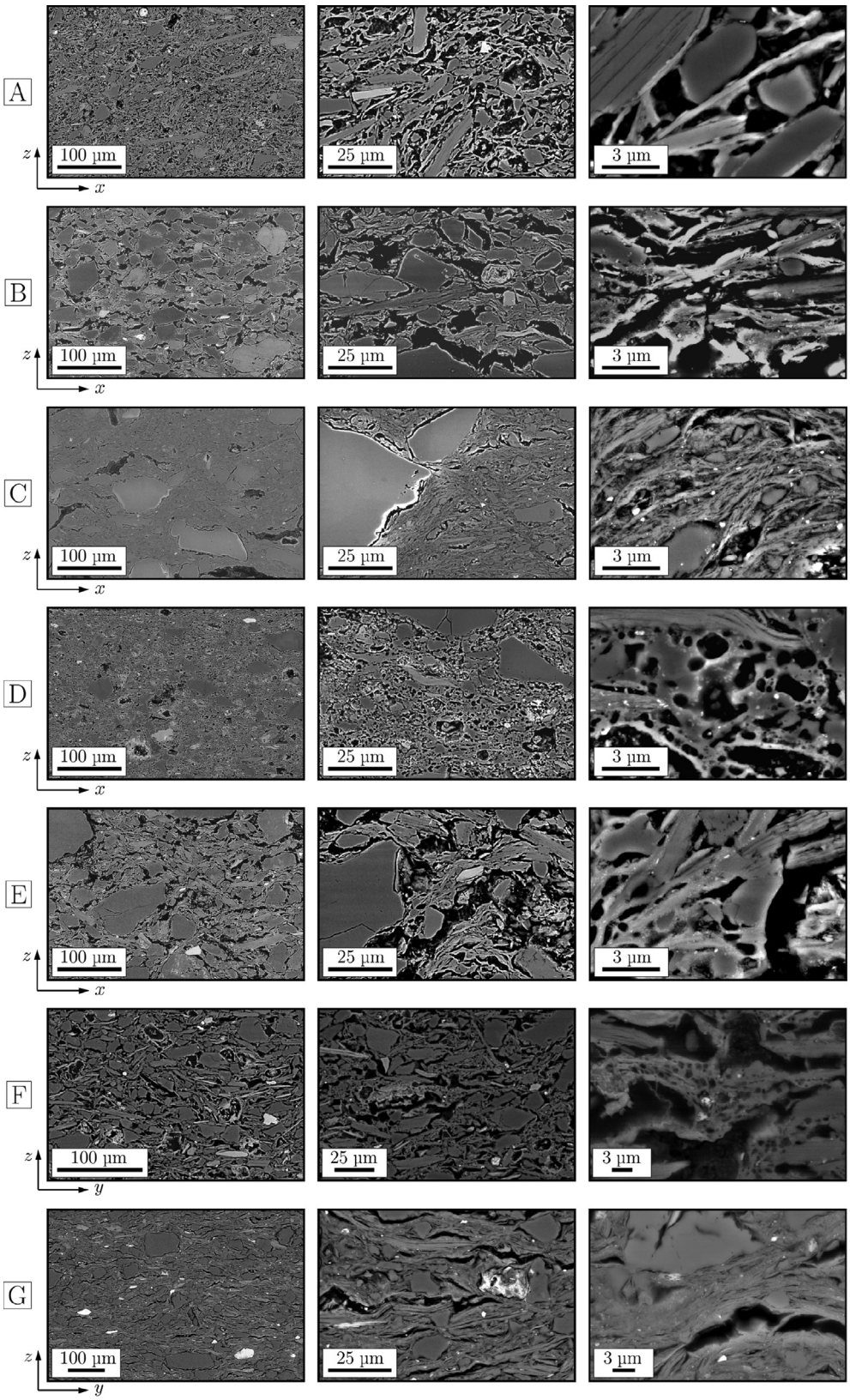

Fig. 1. Backscattered electron images (SEM) of the fired bricks at different magnifications.

volume elements (RVE) [31,68]. The RVEs consist of quasi-homogeneous subdomains with universal phase properties (stiffness, conductivity), so-called material phases, with characteristic size d. Each RVE with characteristic size l must fulfill the inequality condition $d \ll l \ll \mathscr{L}$, with $\mathscr{L}$ as characteristic size of the structure the RVE builds up, or the load applied on the RVE. This scale separation criterion is sufficiently fulfilled, if d is by the factor two to three smaller than l [19], and if l is by a factor of roughly ten smal-

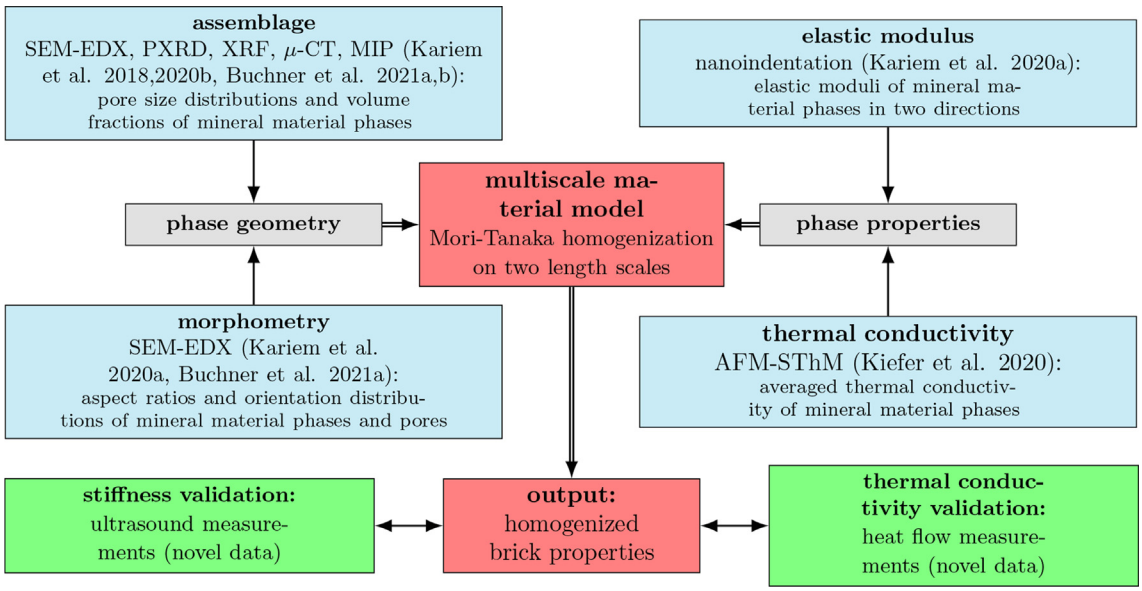

Fig. 2. Flowchart illustrating the modeling strategy and the link to microscopic experiments for phase characterization and macroscopic experiments for model validation. All input data was adopted from published work of our research group, the validation experiments are novel and described in Section 3.

ler than $\mathscr{L}$ [41]. Fired clay brick is modeled by means of two representative volume elements (RVEs) at two observation scales, see Fig. 3(a). At the microscale with characteristic size of $l_{\text{micro}} = 3\ \mu$m, we consider the RVE to consist of a "binding matrix" (which is not further resolved herein) with embedded spheroidal (micro) pores of characteristic size $d_{\text{micro}} \leqslant 1\ \mu$m. The homogenized material at the microscale, denoted as "foam matrix", is considered as matrix phase at the next observation scale, the mesoscale, with characteristic size of $l_{\text{meso}} = 300\ \mu$m, which is by factor 100 larger than l_{micro}. There, the foam matrix is considered to host spheroidal mineral grains (quartz, feldspar, muscovite, Fe-Mg mica) and the remaining (meso)pores with characteristic size $1\ \mu\text{m} < d_{\text{meso}} \leq 150\ \mu$m. Grains or pores with characteristic size of more than 150 μm are absent in the considered bricks. If such large grains (e.g. due to

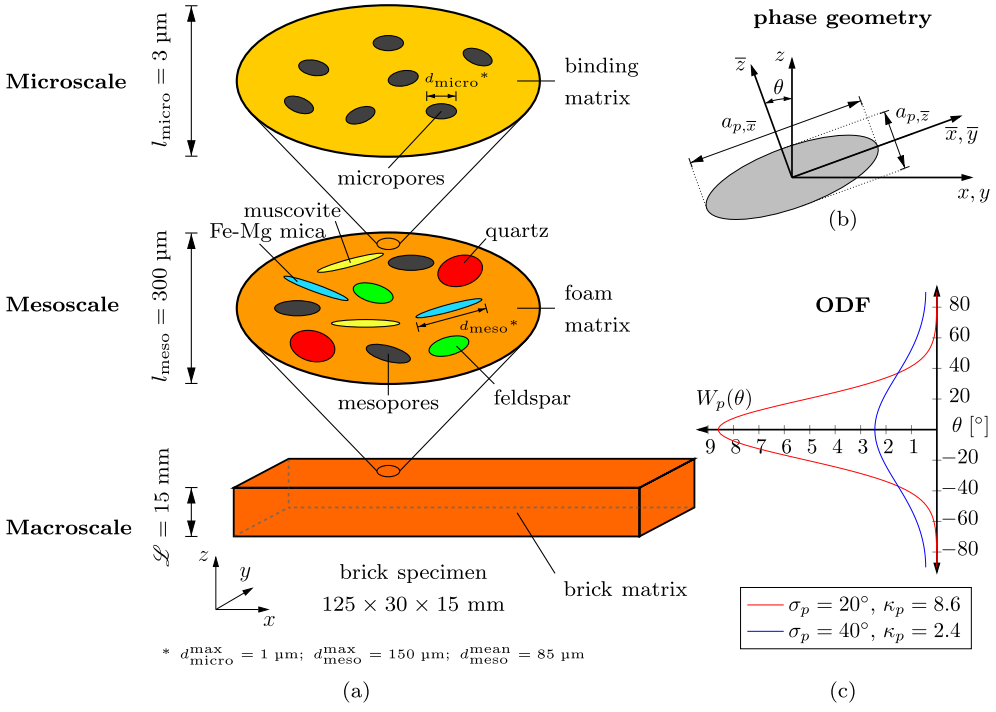

Fig. 3. (a) Two-scale micromechanics model: microscale (scale I) with oriented spherical micropores embedded in a transversely isotropic binding matrix (x-y plane denotes isotropic plane), mesoscale (scale II) with oriented spheroidal material phases (mesopores, quartz, feldspar, muscovite, and Fe-Mg mica) embedded in a foam matrix homogenized at the microscale; (b) Individual phases (index p) are considered as spheroids, characterized by the aspect ratio $X_p = a_{p,\overline{x}}/a_{p,\overline{z}}$, and by a preferential orientation along the x-y plane according to the orientation distribution function (ODF) $W_p(\theta)$, whereby θ denotes the zenith angle between the global z and the local $\overline{z}$ axes. The spheroid's orientation along the azimuth angle φ is considered uniformly distributed; (c) Realization of orientation distribution function $W_p(\theta)$ according to Eq. (1) for two distribution parameters $\kappa_p = \{2.4, 8.6\}$, which correspond to standard deviation σ_p of angle θ amounting to $\sigma_p = \{20°, 40°\}$.

addition of temper) or pores (e.g. due to addition of pore forming additives) exist, introduction of another RVE on a separate observation scale is reasonable [38]. The homogenized material at the mesoscale, denoted as "brick matrix", represents the (homogeneous) material of the extruded brick samples with dimensions of $125 \times 30 \times 15$ mm, which are used for almost all the experiments referred to in this paper. The characteristic size of these bricks, $\mathscr{L} = 15$ mm, is by factor 50 larger than l_{meso}, which still satisfies the scale separation criterion mentioned above [41].

All material phases, except the two matrix phases, are considered to exhibit an oblate spheroidal shape with phase-specific aspect ratio $X_p = a_{p,\bar{x}}/a_{p,\bar{z}}$, whereby $a_{p,\bar{x}}$ and $a_{p,\bar{z}}$ denote the axes lengths, see Fig. 3(b). We consider the spheroidal phases (minerals and pores) to exhibit a preferential orientation along the x-y plane, given the extrusion pressure exerted in z-direction, as typically done for clay bricks [43,7,5,36,9]. As for quantifying the phase orientation, we adopt the orientation distribution function (ODF) proposed by Ulm et al. [65], and confirmed as suitable for material phases in bricks by Kiefer et al. [38], which reads as

$$W_p(\theta) = \frac{\kappa_p \cdot \cosh\left(\kappa_p \cos(\theta)\right)}{\sinh(\kappa_p)}, \tag{1}$$

with $0 \leqslant \theta \leqslant \pi$ denoting the zenith angle between the global z and the local phase-specific $\bar{z}$ axes, see Fig. 3(b) for the definition of the axes, and with κ_p denoting the distribution parameter, see Fig. 3(c) for two realizations of W_p. The orientation distribution is symmetric around the average zenith angle $\theta = 0$, which is corroborated experimentally by Buchner et al. [9]. Notably, the orientation distribution along the azimuth angle $0 \leqslant \varphi \leqslant 2\pi$, with the x-axis as reference, is uniform.

2.3. Homogenization of elastic stiffness and thermal conductivity

As for the homogenization of elastic stiffness and thermal conductivity of the multiphase matrix-inclusion-type RVEs depicted in Fig. 3(a), characterized by spheroidal phases with constant aspect ratio (X_r), with transversely isotropic phase properties ($\mathbb{C}_r, \boldsymbol{\lambda}_r$), and with preferential orientation distribution (W_r according to Eq. (1)), the Mori–Tanaka scheme [6,47] is considered appropriate. Thus, the homogenized elastic stiffness tensor $\mathbb{C}^{\text{hom},s}$ of scale s (standing for micro and meso, respectively) reads as [68,42]

$$\mathbb{C}^{\text{hom},s} = \sum_r f_r^s \int_0^{\pi} \int_0^{2\pi} W_r(\theta) \mathbb{C}_r : \mathbb{A}_r(\varphi, \theta; X_r) \frac{\sin(\theta)}{4\pi} \mathrm{d}\varphi \mathrm{d}\theta, \tag{2}$$

with f_p^s denoting the scale-specific phase volume fraction, $\mathbb{C}_p$ as phase stiffness of the linear elastic phases, and $\mathbb{A}_p$ as fourth-order phase strain concentration tensor. The latter tensor follows from matrix-inclusion problems (Eshelby problems [23]), where a single inclusion, representing the RVE-related phase p is embedded in an infinite matrix with stiffness equal to the one of the binding matrix (for all phases at the microscale) or the foam matrix (at the mesoscale) and reads as [68,42]

$$\mathbb{A}_p(\overline{\varphi}, \overline{\theta}; X_p) = \left[\mathbb{I} + \mathbb{P}_p(\overline{\varphi}, \overline{\theta}; X_p) : (\mathbb{C}_p - \mathbb{C}_m)\right]^{-1} : \left[\sum_r f_r^s \int_0^{\pi} \int_0^{2\pi} W_r(\theta) \left[\mathbb{I} + \mathbb{P}_r(\varphi, \theta; X_r) : (\mathbb{C}_r - \mathbb{C}_m)\right]^{-1} \frac{\sin(\theta)}{4\pi} \mathrm{d}\varphi \mathrm{d}\theta\right]^{-1}, \tag{3}$$

with $\mathbb{P}_p$ as fourth-order Hill tensor, see Mura [50] and Hill [32] for tensor components, and $\mathbb{I}$ as fourth-order identity tensor defined as $I_{ijkl} = 1/2\left(\delta_{ik}\delta_{jl} + \delta_{il}\delta_{jk}\right)$, whereby δ_{ij} is the Kronecker delta. As for the homogenized stiffness $\mathbb{C}^{\text{hom,micro}}$ at the microscale, Eqs. (2) and (3) are evaluated for two material phases, $p, r \in \{\text{bindingmatrix}, \text{micropores}\}$ and $\mathbb{C}_m = \mathbb{C}_{\text{bindingmatrix}}$; for homogenization of $\mathbb{C}^{\text{hom,meso}}$ at the mesoscale, six material phases are considered $p, r \in \{\text{foammatrix}, \text{mesopores}, \text{quartz}, \text{feldspar}, \text{muscovite}, \text{Fe} - \text{Mg mica}\}$ and $\mathbb{C}_m = \mathbb{C}_{\text{foammatrix}}$, see Fig. 3. Given the multiscale setting, $\mathbb{C}_{\text{foammatrix}} = \mathbb{C}^{\text{hom,micro}}$. Notably, phase orientation distributions given by $W_p(\theta)$ according to Eq. (1) render integration in Eqs. (2) and (3) along the surface of the unit sphere necessary. Therefore, azimuth angle φ and zenith angle θ are integration variables and run along the surface of the unit sphere, and $\overline{\varphi}, \overline{\theta}$ stand for fixed orientation angles. The homogenized mesoscale stiffness tensor $\mathbb{C}^{\text{hom,meso}}$ is non-symmetric, a well-known shortcoming of the Mori–Tanaka scheme for non-spherical phases exhibiting non-isotropic phase stiffnesses. As a remedy, $\mathbb{C}^{\text{hom,meso}}$ is symmetrized, $\mathbb{C}^{\text{hom,meso}}_{\text{sym}} = \frac{1}{2}\left[\mathbb{C}^{\text{hom,meso}} + \left(\mathbb{C}^{\text{hom,meso}}\right)^T\right]$, which represents a very accurate approximation of the symmetric Mori–Tanaka scheme according to Sevostianov and Kachanov [59].

The homogenized thermal conductivity tensor $\boldsymbol{\lambda}^{\text{hom},s}$ for scale $s \in \{\text{micro}, \text{meso}\}$ reads, by analogy to stiffness homogenization rule (2), as [27,38]

$$\boldsymbol{\lambda}^{\text{hom},s} = \sum_r f_r^s \int_0^{\pi} \int_0^{2\pi} W_r(\theta) \boldsymbol{\lambda}_r \cdot \boldsymbol{A}_r(\varphi, \theta; X_r) \frac{\sin(\theta)}{4\pi} \mathrm{d}\varphi \mathrm{d}\theta, \tag{4}$$

with $\boldsymbol{\lambda}_p$ as phase conductivity tensor and with $\boldsymbol{A}_p$ as second-order concentration tensor, resulting from thermal matrix-inclusion problems, by analogy to the elastic counterpart Eq. (3), as [27,38]

$$\mathbf{A}_p(\overline{\varphi}, \overline{\theta}; X_p) = \left[\mathbf{1} + \boldsymbol{P}_p(\overline{\varphi}, \overline{\theta}; X_p) \cdot (\boldsymbol{\lambda}_p - \boldsymbol{\lambda}_m)\right]^{-1} \cdot \left[\sum_r f_r \int_0^{\pi} \int_0^{2\pi} W_r(\theta) \left[\mathbf{1} + \boldsymbol{P}_r(\varphi, \theta; X_r) \cdot (\boldsymbol{\lambda}_r - \boldsymbol{\lambda}_m)\right]^{-1} \frac{\sin(\theta)}{4\pi} \mathrm{d}\varphi \mathrm{d}\theta\right]^{-1}, \tag{5}$$

with $\boldsymbol{P}_p$ denoting the second-order Hill tensors for thermal conductivity of phase p, given in full detail in Kiefer et al. [38], and with $\mathbf{1}$ as second-order identity tensor with components being equal to Kronecker delta δ_{ij}. By analogy, $\boldsymbol{\lambda}_m = \boldsymbol{\lambda}_{\text{bindingmatrix}}$ for conductivity homogenization at the microscale and $\boldsymbol{\lambda}_m = \boldsymbol{\lambda}_{\text{foammatrix}} = \boldsymbol{\lambda}^{\text{hom,micro}}$ for homogenization at the mesoscale, see Fig. 3.

Stiffness and conductivity homogenization based on Eqs. (2)–(5) require quantitative input data on phase assemblage in terms of volume fractions f_p^s, phase morphometry (aspect ratios X_p and orientation distribution parameters κ_p), phase stiffnesses (stiffness tensors $\mathbb{C}_p$), and phase conductivites (conductivity tensors $\boldsymbol{\lambda}_p$). For the seven brick compositions A-G, assemblage and morphometry of minerals (quartz, feldspar, muscovite, Fe-Mg mica) and pores (micropores and mesopores) are discussed in the following Section 2.4. Phase properties of the minerals are considered universal, as discussed in Section 2.5, while the ones of the binding matrix are considered to depend on the composition, as discussed in Section 2.6.

2.4. Phase assemblage and phase morphometry

Quantification of phase assemblage is discussed first. To quantify the porosity as well as the corresponding pore size distribution for distinguishing micropores from mesopores, we rely on published results from a multitechnique testing program, applying high-resolution μ-CT scanning, SEM imaging, and MIP testing on the seven studied bricks [34,10]. μ-CT scanning with voxel sizes of 1.2 μm allowed for determination of pores down to 5.5 μm, SEM imaging allowed for resolving pores with dimensions > 700 nm, and MIP was used for quantification of nanometer-sized pores. The resulting phase volume fractions f_p^{meso} of micropores with dimensions $\leqslant 1$ μm and mesopores with

dimensions $> 1\ \mu$m, according to our micromechanics representation of Fig. 3(a), range from roughly 10 % to 20 %, and from 8 % to 30 %, respectively, see Fig. 5. As for the phase volume fractions of the four mineral grains (quartz, feldspar, muscovite, Fe-Mg mica) for all seven bricks, we rely on published results from SEM-EDX and powder X-ray diffraction (PXRD), see Appendix A for the latter [36,9]. The largely automated characterization protocol results in so-called "phase images", see Fig. 4 for examples on brick B and E. These images provide detailed information about the brick's microstructure, thereby giving access to mineral grains with characteristic size down to approximately 1 μm. The remaining solid volume was considered as binding matrix, which consists of small grains ($\leqslant 1\ \mu$m) and an amorphous phase "gluing" the other material phases together. The binding matrix volume fractions range from 30 % (for brick F) to 53 % (for brick D), quartz occupies up to 21 % (whereby we distinguish large from small quartz grains with threshold diameter of ten microns as descibed in detail in Subsection 2.5), while the volume fraction of the other minerals amounts to a maximum of 11 %, see Fig. 5. As for computation of scale-specific phase volume fractions appearing in Eqs. (2)–(5), the volume fraction of the foam matrix is assigned according to $f^{\text{meso}}_{\text{foammatrix}} = f^{\text{meso}}_{\text{micropores}} + f^{\text{meso}}_{\text{bindingmatrix}}$, and the microscale-related volume fractions of micropores and binding matrix, $f^{\text{micro}}_{\text{p}}$, read as

$$f^{\text{micro}}_{\text{micropores}} = \frac{f^{\text{meso}}_{\text{micropores}}}{f^{\text{meso}}_{\text{foammatrix}}}, \qquad f^{\text{micro}}_{\text{bindingmatrix}} = \frac{f^{\text{meso}}_{\text{bindingmatrix}}}{f^{\text{meso}}_{\text{foammatrix}}}. \tag{6}$$

Phase images from SEM-EDX further allowed for quantifying phase morphometries [36,9]. To do so, the authors approximated all visible mineral grains and mesopores by spheroids with aspect ratios $X_p = a_{p\bar{x}}/a_{p\bar{z}}$, see Fig. 3(b) for the definition and Table 1 for the average aspect ratios used for homogenization. Collecting the measured zenith angles θ of each individual spheroidal grain or pore, allows for quantifying the phase-specific orientation distributions. The average of the measured zenith angles for all phases in all seven compositions is very close to zero [9]. The standard deviations, in turn, are phase-specific as well as brick composition-specific, and range from 15° to 45°, see Table 1. The measured orientation distribution was fitted very accurately by the phase orientation distribution function $W_p(\theta)$ with fitting parameter κ_p, see Eq. (1) for definition of the function and Table 1 for the numerical values of

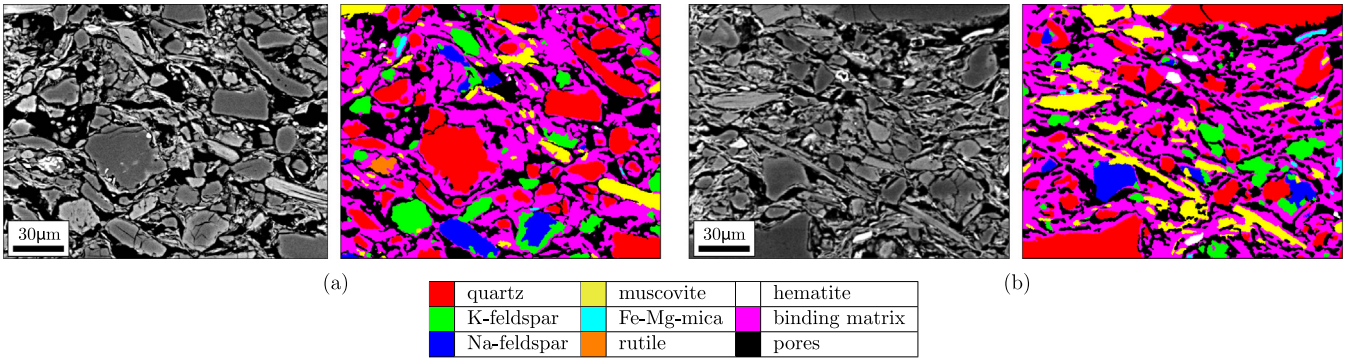

Fig. 4. SEM image and corresponding "phase image" from EDX analyses according to Buchner et al. [9] for (a) brick B, and (b) brick E; K-feldspar and Na-feldspar were considered as single phase herein, hematite and rutitle are neglected.

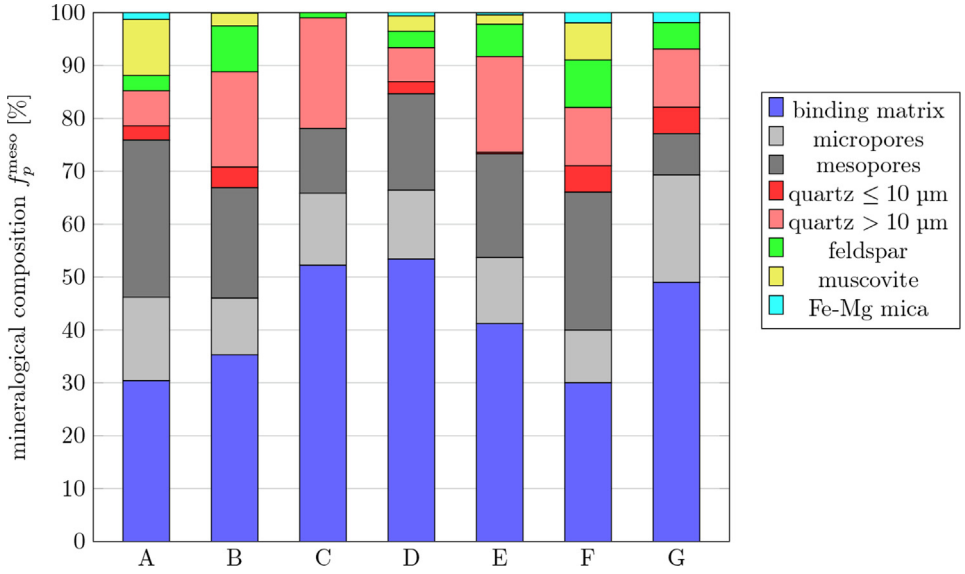

Fig. 5. Microstructural composition of the investigated bricks in terms of mesoscale-related phase volume fractions f_p^{meso}; obtained from combining μ-CT scanning, SEM imaging, and MIP testing for porosity quantification [34,10] and from automated SEM-EDX-PXRD testing for minerals and binding matrix [9,36].

Table 1
Morphometrical description of the spheroidal phases building up the bricks' microstructures, provided by Buchner et al. [9] and Kariem et al. [36]: X_p denotes the average aspect ratio, σ_p is the standard deviation of the measured orientation distribution, and κ_p denotes the corresponding distribution parameter in $W_p(\theta)$.

p =		A	B	C	D	E	F	G
micropores mesopores	X_p	3.22	4.39	3.35	3.28	4.05	4.82	6.07
	σ_p	33.90°	44.27°	29.17°	34.24°	38.96°	31.02°	39.08°
	κ_p	3.24	1.98	4.24	3.17	2.54	3.80	2.52
quartz	X_p	2.48	2.67	2.45	2.66	2.57	3.09	4.01
	σ_p	28.59°	36.12°	37.79°	35.59°	39.71°	35.71°	42.26°
	κ_p	4.39	2.90	2.68	2.98	2.45	2.96	2.18
feldspar	X_p	3.43	2.78	2.07	2.19	2.63	3.40	3.14
	σ_p	32.12°	41.76°	24.74°	32.61°	41.57°	26.98°	39.13°
	κ_p	3.57	2.23	5.73	3.47	2.25	4.88	2.52
muscovite	X_p	3.87	4.24	3.94	4.22	6.65	9.86	–
	σ_p	28.45°	26.78°	23.63°	19.19°	29.29°	23.96°	–
	κ_p	4.43	4.95	6.24°	9.27	4.21	6.08	–
Fe-Mg mica	X_p	3.46	5.66	–	4.80	3.32	10.83	9.21
	σ_p	35.74°	53.10°	–	20.52°	28.39°	16.58°	34.91°
	κ_p	2.96	1.23	–	8.15	4.45	12.29	3.08

κ_p used for homogenization. Given their small size, geometrical features of micropores could not be deduced from the phase images, and are therefore assumed to be identical to those of the mesopores.

2.5. Intrinsic stiffness and conductivity of mineral phases

Regarding quantification of phase stiffness $\mathbb{C}_p$ and phase conductivity λ_p, we first discuss the mineral phases quartz, feldspar, muscovite, and Fe-Mg mica. Their properties are considered to be intrinsic, i.e. they are considered to be independent regarding the brick composition, or in other words, identical for bricks A-G. The stiffness and conductivity of the binding matrix, in turn, is considered to depend on raw material composition, as discussed in the next subsection. The elastic stiffness tensor $\mathbb{C}_p$, as appearing in homogenization rule (2), is considered to be transversely isotropic to stay consistent with the modeling strategy outlined in Section 2.1. The components of its inverse, $\mathbb{D}_p = (\mathbb{C}_p)^{-1}$, are given with respect to the local base frame $\bar{x},\bar{y},\bar{z}$, see Fig. 3(b). Its components read, in Kelvin-Mandel notation, as

$$\mathbb{D}_p = (\mathbb{C}_p)^{-1} = \begin{bmatrix} \frac{1}{E_{p,\bar{x}}} & \frac{-\nu_p}{E_{p,\bar{x}}} & \frac{-\nu_p}{E_{p,\bar{z}}} & 0 & 0 & 0 \\ \frac{-\nu_p}{E_{p,\bar{x}}} & \frac{1}{E_{p,\bar{x}}} & \frac{-\nu_p}{E_{p,\bar{z}}} & 0 & 0 & 0 \\ \frac{-\nu_p}{E_{p,\bar{z}}} & \frac{-\nu_p}{E_{p,\bar{z}}} & \frac{1}{E_{p,\bar{z}}} & 0 & 0 & 0 \\ 0 & 0 & 0 & \frac{1}{2G_{p,\bar{x}\bar{z}}} & 0 & 0 \\ 0 & 0 & 0 & 0 & \frac{1}{2G_{p,\bar{x}\bar{z}}} & 0 \\ 0 & 0 & 0 & 0 & 0 & \frac{1}{2G_{p,\bar{x}\bar{y}}} \end{bmatrix}_{\bar{x},\bar{y},\bar{z}}, \tag{7}$$

with $E_{p,\bar{x}}$ and $E_{p,\bar{z}}$ as direction-dependent elastic moduli, ν_p as Poisson's ratio considered to be direction-independent, $G_{p,\bar{x}\bar{y}} = \frac{E_{p,\bar{x}}}{2(1+\nu_p)}$ as shear modulus in the isotropic plane (resulting from the assumed transverse isotropy). The out of plane shear modulus $G_{p,\bar{x}\bar{z}}$ was estimated through inserting the average of elastic moduli in $\bar{x}$- and $\bar{z}$-direction, $(E_{p,\bar{x}} + E_{p,\bar{z}})/2$, in the equation for isotropic shear modulus, reading as:

$$G_{p,\bar{x}\bar{z}} = \frac{E_{p,\bar{x}} + E_{p,\bar{z}}}{4(1+\nu_p)}. \tag{8}$$

The elastic moduli of quartz, feldspar, and mica phases are derived from published grid nanoindentation results on bricks F and G [35]. Coupling nanoindentation with SEM-EDX allowed for assignment of every single indent to a material phase, thereby giving access to phase-specific elastic moduli. Indents were performed in extrusion direction (x-direction according to Fig. 3(a)) and orthogonal to it (z-direction). Herein, we assume that nanoindentation-derived moduli are identical to the sought phase moduli $E_{p,\bar{x}}$ and $E_{p,\bar{z}}$. This assumption is corroborated by the good agreement between the nanoindentation-derived moduli, summarized in Table 2, and independent results for single-crystal elasticities as discussed in Kariem et al. [35]. A more fundamental analysis of the relation between the nanoindentation-derived stiffness and the phase stiffness, considering the heterogeneity of the indented half space, as well as the orientation and anisotropy of the phases is well beyond the scope of the paper. The stiffness of pores vanishes. The Poisson's ratios ν_p of the mineral phases were adopted from the literature [13], see Table 2.

Table 2
Compilation of phase-specific elastic stiffness and thermal conductivity properties.

		$E_{p,\bar{x}} = E_{p,\bar{y}}$ [2] [GPa]	$E_{p,\bar{z}}$ [2] [GPa]	ν_p [–]	$\bar{\lambda}_p$ [3] $\left[\mathrm{Wm^{-1}K^{-1}}\right]$	$\lambda_{p,\bar{x}}/\lambda_{p,\bar{z}}$ [–]	$\lambda_{p,\bar{x}}$ [4] $\left[\mathrm{Wm^{-1}K^{-1}}\right]$	$\lambda_{p,\bar{z}}$ [4] $\left[\mathrm{Wm^{-1}K^{-1}}\right]$
quartz $\leqslant 10\ \mu$m		113.3	80.8	0.077 [5]	1.07	1.65 [6]	1.26	0.76
quartz $> 10\ \mu$m		0	0	-	1.07	1.65 [6]	1.26	0.76
feldspar		81.2	60.9	0.290 [5]	0.82	1.15 [6]	0.86	0.75
muscovite		62.0	35.5	0.249 [5]	0.75	6.27 [6]	1.38	0.22
Fe-Mg mica		60.0	37.7	0.288 [5]	0.79	6.04 [6]	1.44	0.24
binding matrix	brick F	62.5	45.8	0.200 [7]	1.41	1.36 [8]	1.56	1.16
	brick G	61.2	35.2	0.200 [7]	1.03	1.74 [8]	1.24	0.70

[2] Obtained by nanoindentation measurements, see Kariem et al. [35].
[3] Obtained by SThM measurements, see Kiefer et al. [38].
[4] Calculated according to Eq. (10).
[5] Adopted from Christensen [13].
[6] Adopted from Clauser and Huenges [14].
[7] Inspired by the Poisson's ratio of glass due to high amount of amorphous material in binding matrix, see Buchner et al. [10,9].
[8] Calculated according to Eq. (13).

Despite quartz' very large crystal stiffness, Kilikoglou et al. [39] showed that the bricks elastic modulus decreases with increasing quartz content. Cracks at or close to the quartz surface are very common, particularly for large quartz grains, as confirmed by our own SEM imaging depicted in Fig. 1. These cracks origin from the crystal lattice transformation from α- to β-quartz during firing at a temperature of 573 °C. When cooling down, β-quartz transforms back to α-quartz accompanied by an erratic decrease in volume [48]. This causes large tensile stresses and subsequently cracks along the boundaries of larger quartz grains, considerably weakening the resulting fired brick material [40,63]. Thus, large quartz grains almost certainly do not contribute to the macroscopic material stiffness or even soften the material. Around small quartz grains, cooling-induced boundary stresses are smaller and might be tolerated by the material. Small quartz grains might therefore stiffen the material. In order to consider these phenomena in our model, the stiffness of the quartz phase is set to zero if the minor axis length $a_{\text{quartz},\bar{z}}$ exceeds a threshold size $a_{\text{lim},\bar{z}}$, $E_{\text{quartz},\bar{x}} = E_{\text{quartz},\bar{z}} = 0$ if $a_{\text{quartz},\bar{z}} > a_{\text{lim},\bar{z}}$, while the nanoindentation-derived quartz stiffness is considered otherwise: $E_{\text{quartz},\bar{x}} = 113.3$ GPa, $E_{\text{quartz},\bar{z}} = 80.8$ GPa if $a_{\text{quartz},\bar{z}} \leqslant a_{\text{lim},\bar{z}}$. The SEM images (Fig. 1) show that quartz grains with sizes of a few microns are typically still well-connected to the surrounding material phases, while quartz grains with sizes of a few tens of microns are entirely debonded. This is the motivation to consider the threshold $a_{\text{lim},\bar{z}} = 10\ \mu$m, entailing that most of the quartz volume is considered inactive, see Fig. 5 for the corresponding volume fractions.

Next, the mineral phases' thermal conductivity $\boldsymbol{\lambda}_p$, as appearing in homogenization rule (4), is discussed. By analogy to the phase stiffness Eq. (7), the thermal conductivity tensor is considered to be transversely isotropic. The components read, with respect to the local base frame $\bar{x}, \bar{y}, \bar{z}$, as

$$\boldsymbol{\lambda}_p = \begin{bmatrix} \lambda_{p,\bar{x}} & 0 & 0 \\ 0 & \lambda_{p,\bar{x}} & 0 \\ 0 & 0 & \lambda_{p,\bar{z}} \end{bmatrix}_{\bar{x},\bar{y},\bar{z}}, \tag{9}$$

The components $\lambda_{p,\bar{x}}$ and $\lambda_{p,\bar{z}}$ are back-identified from atomic force microscope-scanning thermal microscopy (AFM-SThM) testing performed on bricks F and G [38]. The testing principle is to move a small tip over a flat surface while keeping the temperature of the tip at a certain level and measuring the energy required to do so. Similar to nanoindentation, parallel SEM-EDX-measured phase images allowed for assignment of measurements to specific material phases, and mineral phases are shown to be – in good approximation – similar for mix F and G. The measured phase conductivity $\bar{\lambda}_p$ is considered as the geometrical average of tensor components $\lambda_{p,\bar{x}}$ and $\lambda_{p,\bar{z}}$ in different spatial directions [52], implying

$$\bar{\lambda}_p = \sqrt[3]{\lambda_{p,\bar{x}}^2 \lambda_{p,\bar{z}}}. \tag{10}$$

We rely on literature data regarding the thermal conductivity ratios $\lambda_{p,\bar{x}}/\lambda_{p,\bar{z}}$ which amount to 1.65, 1.15, 6.27, and 6.04 for quartz, feldspar, muscovite, and Fe-Mg mica, respectively [14], see Table 2. Corresponding direction-dependent thermal conductivities $\lambda_{p,\bar{x}}$ and $\lambda_{p,\bar{z}}$ then follow from combining the ratios with the rearranged average rule (10) under consideration of the measured values $\bar{\lambda}_p$, see Table 2 for numerical values. The thermal conductivity of pores vanishes.

2.6. Composition-dependent stiffness and conductivity of binding matrix

The binding matrix phase in our micromechanics model pools all microstructural features which could not be resolved by means of nanoindentation [35] or thermal microscopy [38]. In contrast to the elastic and thermal behavior of the mineral phases discussed before, the properties of the binding matrix phase are thus mix-dependent, i.e. by design different for the different bricks. Experimental insight from nanoindentation [35] or thermal microscopy [38], however, is only available for bricks F and G. The available experimental data indicate that the nanoindentation-derived stiffness (particularly the elastic modulus in z direction, $E_{\text{bindingmatrix},\bar{z}}$) and the thermal microscopy-derived conductivity $\bar{\lambda}_{\text{bindingmatrix}}$, respectively, are considerably higher for brick F compared to brick G, see Table 2.

Next, we aim at quantification of the stiffness and conductivity of the binding matrix in bricks A-E. Therefore, we consider that the different chemical composition is responsible for the observed differences regarding the mechanical properties of the binding matrix, and focus on the vitrification of the brick, i.e. the fusing of mineral into glassy non-crystalline microstructures. Pronounced vitrification for clays fired below 1000 °C is observed if the raw clays contain large amounts of carbonates in form of calcite and dolomite [17,62,58]. Calcite and dolomite decompose to MgO and CaO, accompanied by the release of CO_2 [17,21]. The alkaline earth metal oxides MgO and CaO aid the vitrification process, resulting in the formation of amorphous calcium-aluminosilicate phases at the applied firing temperature [60,70]. CaO + MgO content from X-ray fluorescence spectroscopy (XRF) measurements was taken as indicator for calcite and dolomite in the raw clays, as reliable XRF results are available for all seven bricks in Kariem et al. [36] and Buchner et al. [10]. The XRF-derived metal oxide mass fraction of CaO + MgO, $m_{\text{CaO+MgO}}$, corrected by the loss on ignition, amounts to 11 % for clay F but only to 2 % for clay G, indicating that vitrification of brick F is more pronounced than in brick G. Higher vitrification is known to result in higher macroscopic mechanical properties and higher macroscopic conductivity [66,22], which in turn, indicates higher stiffness and conductivity of the binding matrix itself, as further corroborated by results from nanoindentation [35] and from thermal microscopy [38] reported in Table 2. In this context, we fit a straight line to the measured CaO + MgO content of bricks F and G, see Fig. 6, allowing us to quantify the binding matrix properties ($E_{\text{bindingmatrix},\bar{z}}$ and $\bar{\lambda}_{\text{bindingmatrix}}$, respectively) as

$$E_{\text{bindingmatrix},\bar{z}} = 32.79 + 1.18\, m_{\text{CaO+MgO}} \quad [\text{GPa}], \tag{11}$$

$$\bar{\lambda}_{\text{bindingmatrix}} = 0.937 + 0.043\, m_{\text{CaO+MgO}} \quad \left[\text{Wm}^{-1}\text{K}^{-1}\right]. \tag{12}$$

The clay-specific mass fractions $m_{\text{CaO+MgO}}$ for bricks A-E are depicted in Fig. 6.

The elastic modulus in x-direction, in turn, is considered to be composition-independent, since nanoindentation-derived results for mix F and G are virtually similar despite their different vitrification levels, see Table 2. This way, its average $E_{\text{bindingmatrix},\bar{x}} = 61.85$ GPa is considered representative for the binding matrix in all seven bricks. By analogy to the mineral phases, we assume that the stiffness tensor of the binding matrix exhibits transversely isotropic symmetries according to Eq. (7). Given the high content of amorphous material in the binding matrix, see Buchner et al. [9], we assume $\nu_{\text{bindingmatrix}} = 0.20$ for all bricks, inspired by the Poisson's ratio of glass. Finally, the average thermal conductivity $\bar{\lambda}_{\text{bindingmatrix}}$ is translated to their directional counterparts. Therefore, we assume that the ratio of thermal conductivities is equal to the ratio of elastic moduli,

$$\frac{\lambda_{\text{bindingmatrix},\bar{x}}}{\lambda_{\text{bindingmatrix},\bar{z}}} = \frac{E_{\text{bindingmatrix},\bar{x}}}{E_{\text{bindingmatrix},\bar{z}}}. \tag{13}$$

This assumption was inspired by micromechanics-based models for the cross-property relation between elastic modulus and thermal conductivity of porous ceramics investigated by Pabst and Gregorová [53,54], which revealed, in reasonable approximation, a pro-

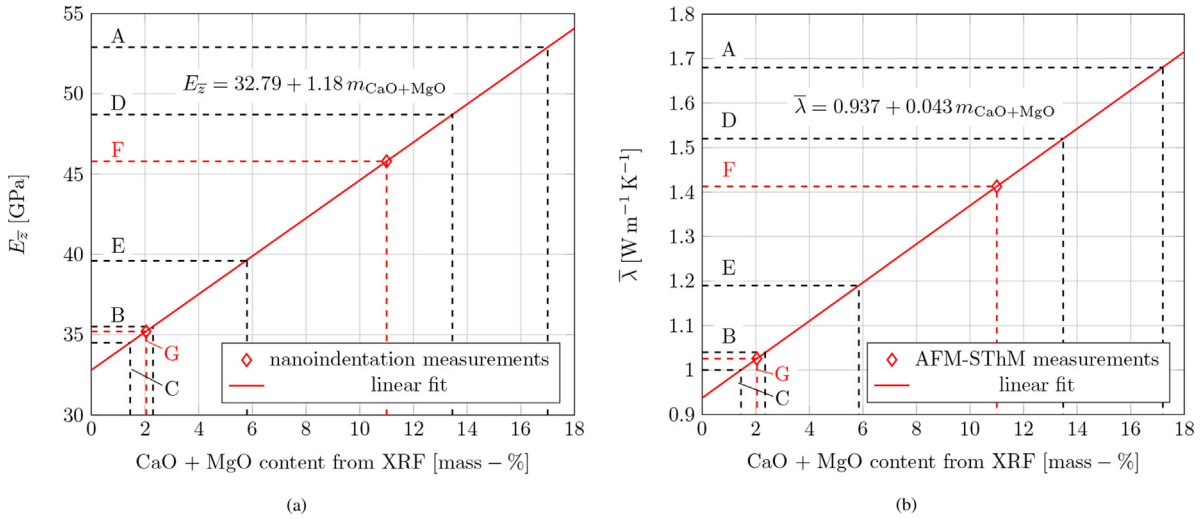

Fig. 6. Experimentally measured properties of the binding matrix with respect to the XRF-derived contents of alkaline earth metal oxides CaO + MgO and corresponding linear fits: (a) elastic modulus in $\bar{z}$-direction from nanoindentation [35] fitted according to Eq. (11); (b) average thermal conductivity from thermal microscopy [38] according to Eq. (12); the depicted XRF values are obtained from Buchner et al. [10] for mixes A-E and Kariem et al. [36] for mixes F and G, and were corrected by the loss on ignition.

portionality between the two quantities. Eq. (13) allows, after insertion into conductivity average rule (10), for back-calculating the sought conductivities $\lambda_{\mathrm{bindingmatrix},\bar{x}}$ and $\lambda_{\mathrm{bindingmatrix},\bar{z}}$.

3. Experiments-based model validation

3.1. Elastic stiffness

3.1.1. Ultrasound measurements

The macroscopic stiffness of the seven bricks was determined by means of novel ultrasound testing, discussed herein. Ultrasound testing enables accurate measurement of the diagonal components of the elastic stiffness tensor of a material [41], by measuring the velocity of an ultrasound wave propagating through the material. Assuming bulk wave propagation, the diagonal components of the elastic stiffness tensor C_{ijij}^{exp} of materials with orthotropic (or higher) symmetry can be calculated as

$$C_{ijij}^{\mathrm{exp}} = \rho\, v_{i,j}^2 = \rho\, v_{j,i}^2, \qquad i,j = x,y,z, \tag{14}$$

with ρ as the material's bulk density and $v_{i,j}$ as wave velocity, whereby the first index i denotes the wave propagation direction and the second index j designates the direction of particle movement caused by the wave. Wave velocities $v_{i,j}$ with indices $i = j$ characterize longitudinal waves and thus axial stiffness components, such with indices $i \neq j$ characterize transversal waves and thus shear stiffness components.

To determine these stiffness values, cuboids with edge lengths between 15 and 50 mm were cut out of the center of the fired clay brick specimens (geometry depicted in Fig. 3(a)). The materials' bulk densities ρ range from $\rho = 1560$ to $\rho = 1977\ \mathrm{kg\,m^{-3}}$, see Table 3 and References [34,10]. Ultrasound measurements were carried out using an ultrasound pulser and signal receiver PR 5077 (Panametrics Inc., USA) in combination with the digital oscilloscope WaveRunner 62Xi (Lecroy Corporation, USA). Both longitudinal and transversal waves with frequency f of 1 MHz (for bricks A to E), and 0.5 MHz (for bricks F and G), respectively, were sent through the specimens, resulting in wave velocities and corresponding stiffness values, see Table 3.

In order to test the sought macroscopic stiffness of the brick matrix, ultrasound wavelengths $\lambda_{i,j} = v_{i,j}/f$ need to be considerably larger [41] than the characteristic size of the RVE at the mesoscale l_{meso} according to Fig. 3(a), which, in turn, has to be by a factor of two to three [19] larger than the characteristic size of grains or pores d, i.e.

$$d < (2 \ldots 3) \times l_{\mathrm{meso}} \ll \lambda_{i,j}. \tag{15}$$

The characteristic size d of the largest mineral grain or pore was estimated for each brick individually on the basis of SEM depicted in Fig. 1, resulting in $d \approx 30\ \mu$m for brick A and D, $d \approx 50\ \mu$m for brick B and F, and $d \approx 100\ \mu$m for brick C, E and G. The calculated ratios $d/\lambda_{i,j}$ are generally smaller than 1/25 for longitudinal waves ($i = j$) and generally smaller than 1/15 for shear waves ($i \neq j$), indicating that the measured stiffness indeed characterizes the brick matrix [41].

Table 3
Brick-specific results from macroscopic testing: bulk density ρ, ultrasound-derived stiffness tensor components C_{ijij}^{exp} (average of two measurements), and heat flow meter-derived thermal conductivity tensor components λ_i^{exp} (mean value and standard deviation based on three to five measurements).

brick	ρ [kg m^{-3}]	C_{xxxx}^{exp} [GPa]	C_{yyyy}^{exp} [GPa]	C_{zzzz}^{exp} [GPa]	C_{yzyz}^{exp} [GPa]	C_{zxzx}^{exp} [GPa]	C_{xyxy}^{exp} [GPa]	λ_x^{exp} [W m^{-1} K^{-1})]	λ_z^{exp} [W m^{-1} K^{-1})]
A	1560	19.97	18.45	8.93	4.57	5.42	8.29	0.648 ± 0.002	0.415 ± 0.002
B	1852	15.12	11.93	5.62	3.41	4.17	6.10	-	0.426 ± 0.004
C	1977	18.29	13.43	6.87	3.88	4.50	6.99	-	0.474 ± 0.004
D	1783	29.00	27.38	16.61	8.47	8.12	12.16	-	0.630 ± 0.004
E	1846	21.68	17.56	9.68	4.89	5.13	7.95	0.798 ± 0.009	0.459 ± 0.008
F	1645	20.01	-	6.81	-	-	-	-	0.475 ± 0.006
G	1930	25.06	-	7.15	-	-	-	-	0.438 ± 0.019

3.1.2. Results and validation

The model-predicted stiffness of all seven bricks is presented and compared to the experimental results from ultrasound testing next. Therefore, stiffness homogenization rule (2) together with strain concentration tensor expression (3) is evaluated for both RVEs depicted in Fig. 3 consecutively, for phase volume fractions and phase morphometries given in Section 2.4, and for phase stiffnesses of minerals (given in Section 2.5) and of the binding matrix (Section 2.6), respectively. The components of the brick-specific homogenized stiffness at the mesoscale, $C_{ijij}^{\mathrm{hom,meso}}$ agree quite well to the ultrasound-derived counterparts $\mathbb{C}_{ijij}^{\mathrm{exp}}$, see Fig. 7. Corresponding mean prediction errors, defined as the mean of the absolute value of brick-specific differences between the average ultrasound-derived stiffness C_{ijij}^{exp} and the model-predicted counterpart $C_{ijij}^{\mathrm{hom,meso}}$, amount to 2.8, 1.5, 1.3, and 0.6 GPa, for the stiffness components $C_{xxxx} = C_{yyyy}, C_{zzzz}, C_{xyxy}$, and $C_{xzxz} = C_{yzyz}$, respectively, which highlight the overall satisfactory model performance.

The model establishes a quantitative link between microstructural features and macroscopic stiffness and thus enables us to understand, in quantitative fashion, the origin of the individual brick stiffness, as discussed in the following paragraphs. Brick D exhibits the largest stiffness, both in axial and shear directions, a fact which is very well captured by our model, see Fig. 7. The high stiffness results from a high amount of binding matrix (volume fraction larger than 50 %, see Fig. 5), which is strongly vitrified given the CaO + MgO content of 13.4 % (see Fig. 6), also visible in the SEM images in Fig. 1. The density of this brick amounts to only 1783 kg m^{-3}, and is thus smaller than the one of several other bricks, see Table 3. The measured and homogenized stiffnesses of bricks A, E, and F are relatively close to each other, with $C_{xxxx} \approx 20$ GPa, despite large differences in their density ranging from 1560 kg m^{-3} for brick A to 1846 kg m^{-3} for Brick E, see Table 3. The stiffness of the high density brick C is compromised by its large content of quartz and by the fact that virtually all of these grains are larger than the threshold diameter of 10 μm, and thus, most likely unable to contribute to the overall stiffness.

Regarding stiffness orthotropy, both model and experiment show that the stiffness ratio C_{xxxx}/C_{zzzz} is close to three for brick F, while it is close to or below two for bricks A, D and E. The higher orthotropy of brick F results from the high aspect ratio of feldspar, muscovite, and Fe-Mg mica in this brick, coupled with their very preferred orientation around the extrusion plane which leads to particularly high distribution parameters κ_p, see Table 1. Notably, the homogenized stiffness is transversely isotropic (with *x*-*y*-plane as plane of isotropy), a consequence of the transversely isotropic, spheroidal phases and their rotationally symmetric orientation distributions (with respect to the *z*-axis). The ultrasound-derived stiffness components C_{xxxx}^{exp}, however, are generally slightly higher than C_{yyyy}^{exp}, see Table 3, indicating some slight orthotropy, particularly for bricks B, C, and E. Orthotropic phase distributions of pores and minerals, which are very likely responsible for the observed differences, are not available from the microstructure characterization experiments.

The model overestimates the ultrasound-derived axial and shear stiffness components of Brick B and C. We already consider that virtually all of the quartz in these bricks is damaged and thus unable to contribute to the macroscopic stiffness, and also that the binding matrix exhibits a very low stiffness itself, given the low CaO + MgO content in these clays. The observed discrepancies may originate from the very poorly vitrified binding matrix, see the SEM images with the highest magnification in Fig. 1, which might result in an even smaller phase stiffness than the CaO + MgO contents would suggest. Moreover, the poor vitrification in bricks B and C might even question the choice of the matrix-inclusion-type morphology which is the basis for the applied Mori–Tanaka homogenization.

3.1.3. Sensitivity study regarding the influence of quartz

Cracks inside and along the surfaces of large quartz grains, induced through a sudden volume decrease of quartz during the cooling process, are incorporated into the model by considering that the stiffness of quartz grains with minor axis length exceeding 10 μm vanishes. Smaller quartz grains, in turn, are considered to remain perfectly bonded to the surrounding matrix phase and exhibit the quartz-intrinsic phase stiffness, such that they are fully contributing to the overall stiffness. The ratio between the volume of perfectly bonded quartz and that of cracked quartz ranges from zero for Brick C to 0.45 for Brick F. To study the stiffening or weakening effect of quartz grains for our seven brick composition in more detail, we herein study two limit cases: either *all* quartz grains are intact and exhibit the crystal-intrinsic stiffness or *all* quartz grains are cracked and considered as phases with vanishing stiffness. This way, bounds for the macroscopic brick stiffness are obtained, see Fig. 8. The ranges of modeling results between these limit cases are illustrated as columns. The upper bound, corresponding to uncracked quartz grains, significantly overestimates the ultrasound-derived stiffness in all compositions, which illus-

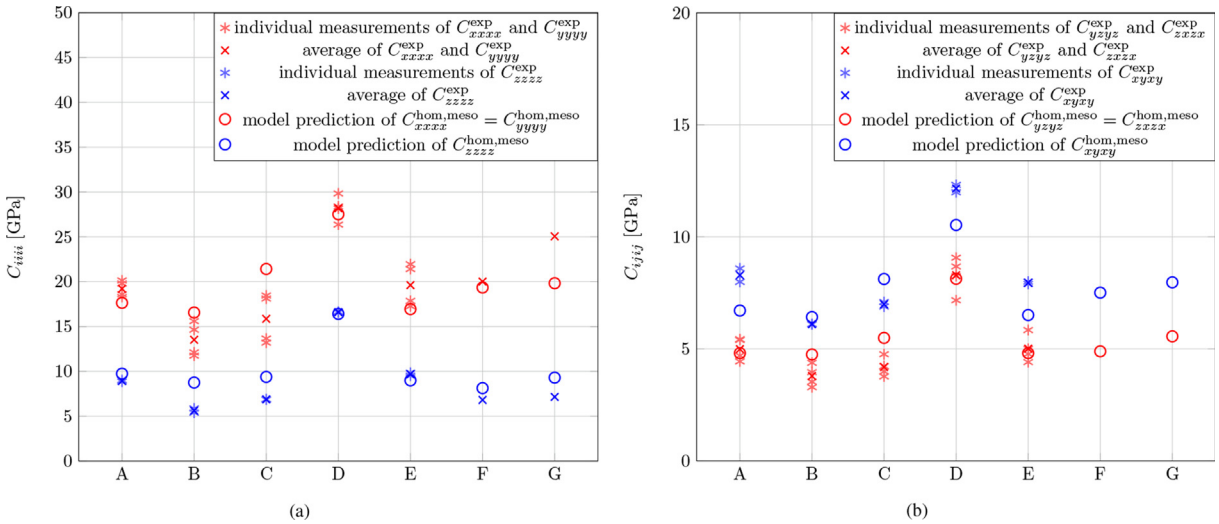

Fig. 7. Comparison of model-predicted and experimentally measured macroscopic stiffness tensor components: (a) axial components, (b) shear components.

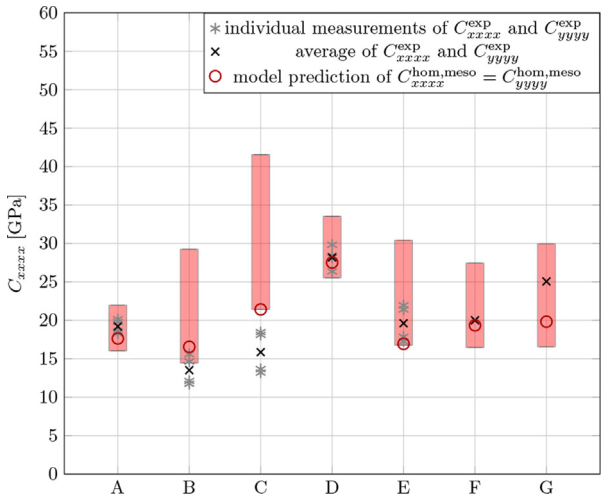

Fig. 8. Bounds for the homogenized brick stiffness considering two limit cases: *all* quartz grains are intact (upper bound) or *all* quartz grains are cracked (lower bound). The red columns indicate the range between the upper and the lower bounds.

trates the importance of considering the weakening effect of the cracks. The lower bound, corresponding to cracked quartz grains, underestimates the (average) ultrasound-derived stiffness for most compositions, which illustrates, that some of the quartz is stiffening the material. Model predictions using the 10 μm threshold, depicted by red circles in Fig. 8, lead to satisfactory model performance. A physically more rigorous representation of quartz cracking through quantifying cooling-induced eigenstrains in quartz and their effect on the bond between quartz and the surrounding matrix is beyond the scope of the paper, but renders an interesting extension of the model in the future.

3.2. Thermal conductivity

3.2.1. Heat flow meter measurements

The macroscopic thermal conductivity of the seven bricks was determined according to ASTMC518-04 [2] and ASTME1530-06 [3] by means of a FOX 50 110 °C (LaserComp, USA) heat flow meter and Pyrex as calibration material. Radially isolated cylindrical samples with diameters of 55 mm are placed between water-cooled Peltier elements, see the scheme depicted in Fig. 9(a). This way, the material is subjected to one-dimensional steady-state heat flow in axial cylinder direction, with fixed temperatures at the hot and cold side amounting to 15 °C and 5 °C, respectively. The brick specimens used for microstructure characterization experiments as well as for the novel ultrasound tests are too small to prepare cylinders with the required dimensions. As a remedy, larger samples measuring $260 \times 58 \times 17$ mm in x, y and z-direction, respectively, were extruded and again fired at 880 °C. The thickness (17 mm) of these specimens is very similar to that of the specimen in Fig. 3 (15 mm), therefore similar extrusion pressures are expected.

This way, we further expect that the phase morphometries (particularly the orientation distributions of minerals and pores) quantified on the smaller samples are still valid. Cylinders with diameter of 55 mm (in x-y-plane) where drilled out of the larger specimens and placed in the heat flow meter to measure the conductivity λ_z^{exp}. Additionally, measurements in x-direction were performed on bricks A and E. In order to prepare the required cylindrical samples with 55 mm diameter (in y-z-plane), four specimens were glued together, as described in Kiefer et al. [38].

The heat flow meter provides total thermal resistances $R_{tot}(t)$, which depend on the sample thickness t, see Fig. 9(b), and include the thermal resistance of the contact between sample and device, denoted R_c. Hence, the material's thermal conductivity reads as

$$\lambda = \frac{t}{R_{tot}(t) - R_c}. \tag{16}$$

Testing multiple thicknesses, achieved by consecutively grinding the samples down to five target thicknesses t (amounting to roughly 16, 12, 9, 6, and 4 mm), allows for calibrating the test setup, as described next. The contact resistance is the total resistance at zero thickness, and it is quantified by linear fitting (after removing potential outliers) of the measured data $R_{tot}(t)$ vs. t, see Fig. 9(b). The resulting thermal conductivities λ_z^{exp} and λ_x^{exp} are given in Table 3, whereby the values for brick F and G were adopted from Kiefer et al. [38]. Notably, the thermal conductivity of bricks remains virtually constant between 0 and 300 °C, see Nguyen and

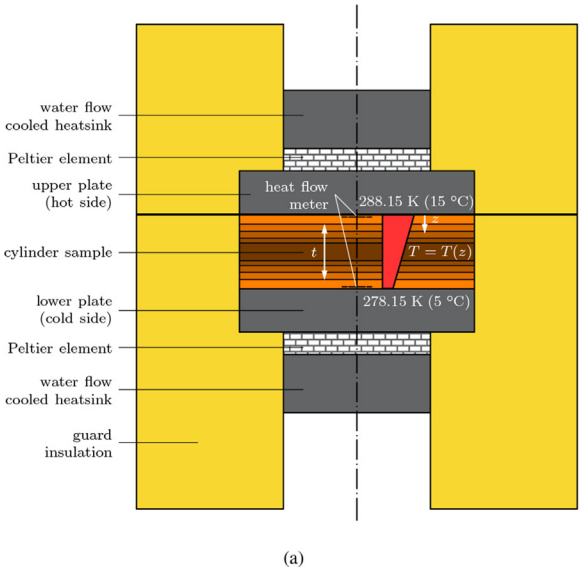

(a)

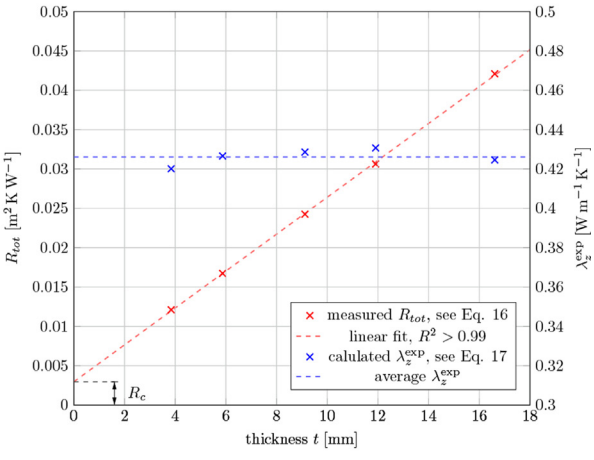

(b)

Fig. 9. Heat flow meter measurements for quantification of macroscopic conductivity: (a) test setup with one-dimensional temperature field, (b) total thermal resistance R_{tot} of brick B measured for different specimen thicknesses t and fitted linearly to determine the thermal contact resistance R_c, allowing for quantification of the sought (thickness-independent) brick conductivity λ_z^{exp}.

Meftah [51], such that temperature gradient-induced measurement inaccuracies can be neglected.

Finally, by analogy to ultrasound testing, we check whether the test setup satisfies the scale separation criterion $d < (2\dots3) \times l_{\text{meso}} \ll \mathscr{L}$ with $\mathscr{L}$ interpreted as the characteristic length of the thermal load. This length reads as [38]

$$\mathscr{L}(\boldsymbol{X}) = \frac{|T(\boldsymbol{X})|}{||\mathbf{GRAD}(T(\boldsymbol{X}))||}, \tag{17}$$

with $T(\boldsymbol{X})$ as macroscopic temperature field, $\boldsymbol{X}$ as corresponding location vector and $\mathbf{GRAD}(\cdot)$ as the macroscopic gradient. Specialization of Eq. (17) for the 1D temperature field inside the heat flow meter, i.e. for the $T(\boldsymbol{X}) = T(z)$ with constant gradient $\Delta T/t$ yields $\mathscr{L} = T(z)/(\Delta T/t)$, whereby $\Delta T = 10$ K. We are interested in computing the smallest length $\mathscr{L}$, which results from considering the minimum temperature $T(z = t) = 278.15$ K and the minimum thickness $t = 4$ mm, resulting in $\mathscr{L} > 111$ mm. As this is much larger than the characteristic length of the RVE at the mesoscale, scale separating is readily satisfied.

3.2.2. Results and validation

As for the comparison of homogenized thermal conductivities, conductivity homogenization rule (4) together with concentration tensor expression (5) is evaluated for both RVEs depicted in Fig. 3 consecutively, for phase volume fractions and phase morphometries given in Section 2.4, and for phase conductivites of minerals (given in Section 2.5) and of the binding matrix (Section 2.6), respectively. The components of the homogenized thermal conductivity $\lambda_i^{\text{hom,meso}}$ agree very well with the experimental counterparts from heat flow measurements, λ_i^{exp}, see Fig. 10. Corresponding mean prediction errors, amount to 0.022 and 0.097 $\text{Wm}^{-1}\text{K}^{-1}$, for the components $\lambda_x = \lambda_y$ and λ_z, respectively. Again, the model performance is very satisfactory for all seven different bricks which further underlines that the micromechanics model is well suited for translating brick-specific microstructural features to macroscopic properties. Notably, the modeled macroscopic conductivity exhibits, by analogy to the homogenized stiffness, transverse isotropic symmetry, which has been confirmed as being a reasonable approximation for fired clay bricks by several authors [5,43,46,7,44].

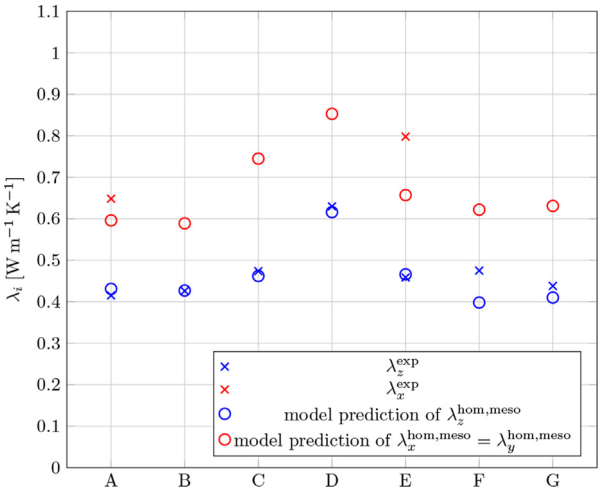

Fig. 10. Validation of the modeled λ-values on basis of multiple thickness heat flow measurements.

The satisfactory model performance provides the motivation to discuss the microstructural origin of the measured brick-specific conductivities. The modeled macroscopic thermal conductivities of the bricks A, B, C, E, F, and G are quite similar, despite large differences of the material densities (Table 3). Conductivity and density are not correlated. Similar observations have been made for other brick compositions by Erker [22] and Gualtieri et al. [29], who established the name "bulk density-thermal conductivity paradox". From a purely macroscopic standpoint, these observation might be indeed unexpected: The proposed microstructure-informed model, in turn, allows for shedding light on this "paradox" and for exploring its microstructural origin. For instance, brick A exhibits the smallest density (Table 3), corresponding to the highest porosity (Fig. 5). The macroscopic thermal conductivity of this brick is substantially increased by high phase conductivity of the binding matrix, resulting from strong vitrification caused by large CaO + MgO content (Fig. 6). Bricks B, C, E, and G, in turn, exhibit very small CaO + MgO contents, and thus a poorly vitrified binding matrix with small phase conductivity. The macroscopic conductivity, however, is high, because these bricks are the ones with high density (Table 3) and thus low porosity (Fig. 5). The extraordinary high macroscopic conductivity of brick D can be explained by a very high content of binding matrix, which is strongly vitrified due to a high content of MgO + CaO.

3.2.3. Sensitivity analysis regarding thermal conductivity of material phases

AFM-SThM-measured thermal conductivities, reported by Kiefer et al. [38] and used herein to feed the model are generally somewhat lower than corresponding values tabulated for single crystals from Clauser and Huenges [14], see Table 4. This is why we herein re-evaluate the model using single crystal data only. The unknown binding matrix conductivity $\overline{\lambda}_{\text{bindingmatrix}}$ is then fitted ("downscaled"), such that the homogenized conductivity $\lambda_z^{\text{hom,meso}}$ matches the brick-specific measured conductivity λ_z^{exp}. This yields fitted binding matrix conductivities amounting to 0.87, 0.43, 0.56, 1.07, 0.56, 0.72, and 0.57 $\text{Wm}^{-1}\text{K}^{-1}$ (for bricks A to G), which are significantly smaller than the AFM-SThM results given in Table 2. Studying the fitting results with respect to the CaO + MgO contents, see Fig. 11, reveals that the binding matrix conductivity increases with increasing amounts of CaO + MgO, thus corroborating the assumption of a vitrification-enhanced matrix conductivity, aided by high contents of CaO and MgO [60,70].

3.3. Cross-property relation between thermal conductivity and elastic modulus

After successfully predicting the brick stiffness and the brick conductivity individually, we herein study the relation between the two quantities. Such cross-property relations (CPRs) have been developed for isotropic porous ceramics in recent years [53,54,64].

Table 4
Thermal conductivity of mineral phases valid for single crystals from Clauser and Huenges [14].

		quartz	feldspar	muscovite	Fe-Mg mica
$\lambda_{p,\bar{x}}$	$\left[\text{Wm}^{-1}\text{K}^{-1}\right]$	10.17	2.68	3.89	3.14
$\lambda_{p,\bar{z}}$	$\left[\text{Wm}^{-1}\text{K}^{-1}\right]$	6.15	2.34	0.62	0.52

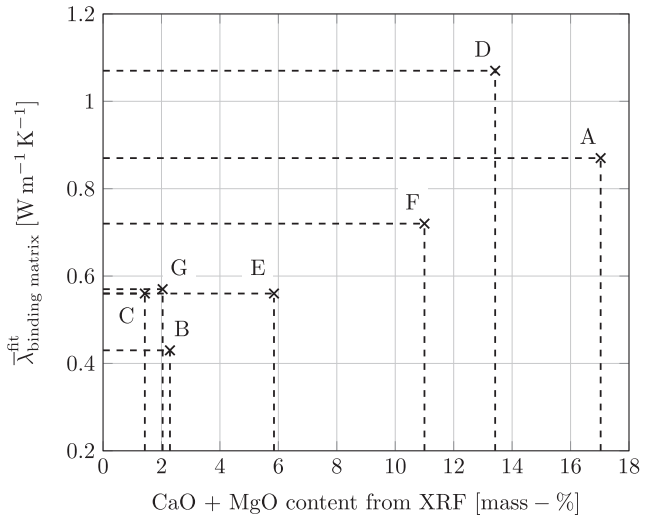

Fig. 11. Fitted ("downscaled") thermal conductivity of the binding matrix with respect to the matrix' CaO + MgO contents, based on tabulated single crystal conductivities for mineral phases from Clauser and Huenges [14].

Therefore, the authors used classical homogenization rules to obtain analytical expressions of the relative elastic modulus E/E_0 and thermal conductivity λ/λ_0 (normalized with respect to the solid modulus E_0 and the solid conductivity λ_0) of the composite material as function of porosity. Herein, we follow Uhlířová et al. [64] and consider four distinct CPRs: the Wiener-Paul CPR and the Hashin–Shtrikman CPR, which both result from the corresponding analytical expressions of upper bounds for modulus and conductivity, as well as a linear CPR and a non-linear (power-law-type) CPR (denoted Pabst-Gregorová CPR) which are both obtained from considering a single spherical inclusion in an infinite solid, see the corresponding plots in Fig. 12.

Next, these purely theoretical CPRs are compared to the CPRs related to the proposed multiscale model. Therefore, E_0 and λ_0 are evaluated considering bricks with vanishing (micro- and meso-) porosity and the properties in $x = y$- and z-direction are related individually. The resulting brick-specific points are close to the theoretical CPRs (see Fig. 12), which may help to gain confidence with the proposed advanced micromechanical approach. The observed deviations, in turn, demonstrate that consideration of (i) several rather than a single solid phase, (ii) matrix-inclusion-type phase interactions in the framework of the Mori-Tananka scheme, (iii) a multiscale micromechanics setting with two RVEs, (iv) a clay-specific morphometry (aspect ratio and orientation of phases), and (v) transversely isotropic microstructural properties, does indeed matter, even for the evaluation of relative cross-property relations. For *predicting* the (absolute) elastic stiffness and thermal conductivity, respectively, capturing the aforementioned characteristic features of brick microstructures into a microstructural model is even essential, as demonstrated by the very satisfactory performance of the proposed multiscale model.

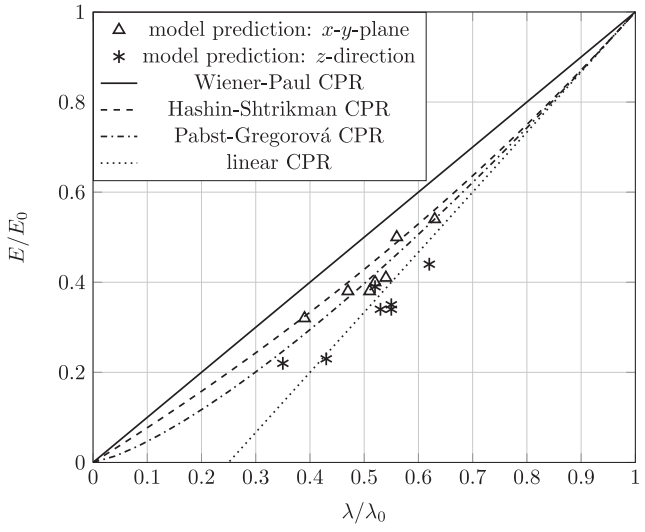

Fig. 12. Comparison of model predictions with existing models for cross-property relations between thermal conductivity and elastic modulus for ceramic materials described in Uhlířová et al. [64].

4. Conclusion and outlook

Elastic stiffness and thermal conductivity of a large variety of extruded and fired (880 °C) clay bricks, made of the most common clayey raw materials in the European brick industry, were modeled in this work. By means of a multiscale continuum micromechanics model, the complex microstructure of clay bricks was resolved down to the micrometer scale, where mineral phases (quartz, feldspar, and micas) and pores can be distinguished from the remaining binding matrix. Mineral and pore phase assemblage and phase morphometry were obtained from extensive microscopic testing [34–36,10,9], and clearly depend on the raw clay composition. The mineral phase stiffness and conductivity, however, are composition-independent and obtained from literature databases, nanoindentation testing [35], and scanning thermal microscopy [38]. Stiffness and conductivity of the binding matrix, in turn, are consiered to increase linearly with increasing carbonate contents of raw clays, as carbonates aid vitrification. Large quartz grains are considered to not contribute to the overall stiffness, given that cracks run along their interfaces.

Homogenized elastic stiffness and homogenized thermal conductivity are very close to independent results from macroscopic ultrasound and heat flow meter testing, respectively. Notably, the good agreement does hold for all seven tested brick compositions, which demonstrates that a unique microstrucural representation in the framework of continuum micromechanics, if evaluated with composition-dependent phase assemblage, phase morphometry and matrix properties, is able to predict the macroscopic behavior of bricks made of very different clays. Thus, the model assumptions are corroborated, particularly (i) the linear increase of the binding matrix properties with the material's carbonate content and (ii) the inability of large quartz with interface cracks to take over any mechanical loads. The successful quantitative upscaling of measured microscopic features to macroscopic brick properties, for seven mineralogically very different bricks, also highlights that neither stiffness nor conductivity are commonly correlated to the brick density, a material behavior previously termed "paradox" [22,29]. The microstructure-informed model proposed herein resolves this paradox, as it quantifies the importance of several other microstructural features beyond the porosity (which defines the density). This way, the model opens the path for effective, physics-based optimization of modern brick products.

The presented micromechanics model is limited to clay mixtures without pore-forming additives (e.g. extruded polystyrene, sawdust and paper sludge) or tempers (e.g. slag, fly ash and quartz sand) and to firing temperatures of 880 °C. In the future, we aim at expanding the model beyond these limitations. Moreover, we aim at rigorously considering cracking around large quartz grains, by means of quantifying tensile eigenstresses resulting from cooling-induced contraction after firing of the clay, by considering interface debonding due to these eigenstresses, and by quantifying

the effect of these debonded interfaces on the macroscopic stiffness. Given the importance of the matrix phase properties for the prediction of the homogenized macroscopic brick properties, future experimental work should focus on characterizing the microscopic properties of the binding matrix and on the link between these properties and the matrix' chemical and mineralogical features.

Data availability

The raw/processed data required to reproduce these findings cannot be shared at this time as the data also forms part of an ongoing study.

Declaration of Competing Interest

The authors declare that they have no known competing financial interests or personal relationships that could have appeared to influence the work reported in this paper.

Acknowledgments

The authors gratefully acknowledge the financial support of the Austrian Research Promotion Agency (FFG, project number 865067), the "Klima- und Energiefonds" Austria, and the industry partner Wienerberger AG for funding the research work through the project 'Innovative Brick 2'. Furthermore, the authors acknowledge TU Wien Bibliothek for financial support through its Open Access Funding Programme, and would like to thank Olaf Lahayne and David Beranek for performing ultrasound measurements as well as Wolfgang Gaggl and Gottfried Früh for performing heat flow measurements.

Appendix A. Mineralogical composition of brick materials

The PXRD-derived mineralogical compositions of the investigated materials is given in Table A.5 for the raw clays as well as the fired bricks (880 °C). Table A.6 shows mineralogical compositions (obtained by PXRD) of the clay fraction ($< 2\ \mu$m) in the raw clays. The data for brick A to E was adopted from Buchner et al. [10] and those for brick F and G was adopted from Kariem et al. [36]. For information about the chemical composition it is referred to the above literature.

References

[1] I. Allegretta, G. Eramo, D. Pinto, A. Hein, The effect of mineralogy, microstructure and firing temperature on the effective thermal conductivity of traditional hot processing ceramics, Appl. Clay Sci. 135 (2017) 260–270, https://doi.org/10.1016/j.clay.2016.10.001. URL https://doi.org/10.1016/j.clay.2016.10.001.
[2] ASTMC518-04. Standard test method for steady-state thermal transmission properties by means of the heat flow meter apparatus. 2004. doi: 10.1520/C0518-04. http://www.astm.org/cgi-bin/resolver.cgi?C518.
[3] ASTME1530-06. Standard test method for evaluating the resistance to thermal transmission of materials by the guarded heat flow meter technique. 2006. doi: 10.1520/E1530-06. http://www.astm.org/cgi-bin/resolver.cgi?E1530.
[4] T.K. Bader, K. Hofstetter, C. Hellmich, J. Eberhardsteiner, Poromechanical scale transitions of failure stresses in wood: from the lignin to the spruce level, Jounal of Applied Mathematics adn Mechanics 90 (10–11) (2010) 750–767, https://doi.org/10.1002/zamm.201000045. URL https://doi.org/10.1002/zamm.201000045.
[5] R. Bartusch, F. Händle, Extrusion in Ceramics, Springer-Verlag, 2007.
[6] Y. Benveniste, A new approch to the application of Mori-Tanaka's theory in composite materials, Mech. Mater. 6 (1987) 147–157, https://doi.org/10.1016/0167-6636(87)90005-6. URL https://doi.org/10.1016/0167-6636(87)90005-6.
[7] J. Bourret, N. Tessier-Doyen, R. Guinebretiere, E. Joussein, D. Smith, Anisotropy of thermal conductivity and elastic properties of extruded clay-based materials: Evolution with thermal treatment, Appl. Clay Sci. 116–117 (2015) 150–157, https://doi.org/10.1016/j.clay.2015.08.006. URL https://doi.org/10.1016/j.clay.2015.08.006.
[8] L. Brown, P.G. Allison, F. Sanchez, Use of nanoindentation phase characterization and homogenization to estimate the elastic modulus of heterogeneously decalcified cement pastes, Materials & Design 142 (2018)

Table A.5
PXRD-derived mineralogical composition of the investigated raw materials as well as fired (880 °C) bricks from Buchner et al. [10] (A-E) and Kariem et al. [36] (F and G). Relative quantity: **** = very abundant; *** = abundant; ** = medium; * = scarce; + = rare; - = not detected; n.s. = not specified.

	A		B		C		D		E		F		G	
	raw	fired	raw	fired	raw	fired	raw	fired	raw	fired	raw	fired	raw	fired
quartz	**	**	****	****	****	****	**	**	***	***	***	***	****	****
K-feldspar	*	*	*	*	*	*	*	*	*	*	*	*	*	-
plagioclase	*	*	*	*	+	-	*	**	*	*	*	*	*	*
muscovite	**	*	*	*	*	*	**	*	*	*	**	*	**	+
paragonite	*	-	-	-	-	-	-	-	-	-	*	-	-	-
chlorite	*	-	+	-	-	-	*	-	*	-	*	-	*	-
kaolinite	-	-	-	-	**	-	-	-	*	-	-	*	-	-
calcite	*	-	-	-	-	-	*	-	*	-	*	-	-	-
dolomite	*	-	-	-	-	-	*	-	+	-	*	-	-	-
augite	-	*	-	-	-	-	-	*	-	-	-	-	-	-
hematite	-	*	-	*	-	-	-	*	-	*	-	*	-	*
gehlenite	-	*	-	-	-	-	-	*	-	-	-	*	-	-
hornblende	-	-	+	-	-	-	-	-	-	-	-	-	-	-
heulandite	-	-	-	-	-	-	+	-	-	-	-	-	-	-
clay minerals + amorphous	**	-	**	-	**	-	***	-	**	-	n.s.	-	n.s.	-
amorphous	-	**	-	**	-	**	-	**	-	**	-	***	-	***

Table A.6
PXRD-derived mineralogical composition of the clay fraction ($< 2\ \mu$m) of the investigated materials before firing from Buchner et al. [10] (A-E) and Kariem et al. [36] (F and G). Relative quantity: **** = very abundant; *** = abundant; ** = medium; * = scarce; + = rare; - = not detected.

	A	B	C	D	E	F	G
smectite	***	***	**	****	**	***	-
illite	***	**	**	**	***	**	**
chlorite	*	-	-	-	*	*	*
kaolinite	*	**	****	*	*	*	**
vermiculite	-	*	-	*	*	+	****

308–318, https://doi.org/10.1016/j.matdes.2018.01.030. ISSN 0264-1275. URL https://www.sciencedirect.com/science/article/pii/S0264127518300388.
[9] T. Buchner, T. Kiefer, W. Gaggl, L. Zelaya-Lainez, J. Füssl, Automated morphometrical characterization of material phases of fired clay bricks based on scanning electron microscopy, energy dispersive x-ray spectroscopy and powder x-ray diffraction, Constr. Build. Mater. 288 (2021) 122909, https://doi.org/10.1016/j.conbuildmat.2021.122909. ISSN 0950-0618. URL https://www.sciencedirect.com/science/article/pii/S0950061821006693.
[10] T. Buchner, T. Kiefer, L. Zelaya-Lainez, W. Gaggl, T. Konegger, J. Füssl, A multitechnique, quantitative characterization of the pore space of fired bricks made of five clayey raw materials used in european brick industry, Appl. Clay Sci. 200 (2021) 105884, https://doi.org/10.1016/j.clay.2020.105884. ISSN 0169-1317. URL https://www.sciencedirect.com/science/article/pii/S016913172030449X.
[11] S. Calderón, C. Sandoval, O. Arnau, Shear response of partially-grouted reinforced masonry walls with a central opening: Testing and detailed micro-modelling, Materials & Design 118 (2017) 122–137, https://doi.org/10.1016/j.matdes.2017.01.019. ISSN 0264-1275. URL https://www.sciencedirect.com/science/article/pii/S0264127517300199.
[12] L. Casnedi, G. Pia, Morphology influence on elastic deformation behaviour of high porous ceramics. experimental and phenomenological model predictions, Ceram. Int. 47 (16) (2021) 23368–23375, https://doi.org/10.1016/j.ceramint.2021.05.052. ISSN 0272-8842. URL https://www.sciencedirect.com/science/article/pii/S0272884221014371.
[13] N.I. Christensen, Poisson's ratio and crustal seismology, Journal of Geological Research 101 (B2) (1996) 3139–3156, https://doi.org/10.1029/95JB03446. URL https://doi.org/10.1029/95JB03446.
[14] C. Clauser and E. Huenges. Rock Physics and Phase Relations: A Handbook of Physical Constants, Chapter: Thermal Conductivity of Rocks and Minerals. American Geophysical Union, 1995.
[15] C. Coletti, G. Cultrone, L. Maritana, C. Mazzoli, Combined multi-analytical approach for study of pore system in bricks: How much porosity is there?, Mater Charact. 121 (2016) 80–92, https://doi.org/10.1016/j.matchar.2016.09.024. URL https://doi.org/10.1016/j.matchar.2016.09.024.
[16] C. Coletti, G. Cultrone, L. Maritana, C. Mazzoli, How to face the new industrial challenge of compatible, sustainable brick production: Study of various types of commercially available bricks, Appl. Clay Sci. 124–125 (2016) 219–226, https://doi.org/10.1016/j.clay.2016.02.014. URL https://doi.org/10.1016/j.clay.2016.02.014.
[17] G. Cultrone, E. Sebastián, K. Elert, M.J. de la Torre, O. Cazalla, C. Rodriguez-Navarro, Influence of mineralogy and firing temperature on the porosity of bricks, J. Eur. Ceram. Soc. 24 (2004) 547–564, https://doi.org/10.1016/S0955-2219(03)00249-8. URL https://doi.org/10.1016/S0955-2219(03)00249-8.
[18] M. Dondi, F. Mazzanti, P. Principi, M. Raimondo, G. Zanarini, Thermal conductivity of clay bricks, J. Mater. Civ. Eng. 16 (1) (2004) 8–14, https://doi.org/10.1061/(ASCE)0899-1561(2004)16:1(8). URL https://ascelibrary.org/doi/abs/10.1061/%28ASCE%290899-1561%282004%2916%3A1%288%29.
[19] W. Drugan, J. Willis, A micromechanics-based nonlocal constitutive equation and estimates of representative volume element size for elastic composites, J. Mech. Phys. Solids 44 (4) (1996) 497–524, https://doi.org/10.1016/0022-5096(96)00007-5. ISSN 0022-5096. URL https://www.sciencedirect.com/science/article/pii/0022509696000075.
[20] L. Eberhardsteiner, J. Füssl, B. Hofko, F. Handle, M. Hospodkaa, R. Blab, H. Grothe, Influence of asphaltene content on mechanical bitumen behavior: experimental investigation and micromechanical modeling, Mater. Struct. 48 (2015) 3099–3112, https://doi.org/10.1617/s11527-014-0383-7. URL https://doi.org/10.1617/s11527-014-0383-7.
[21] K. Elert, G. Cultrone, C.R. Navarro, E.S. Pardo, Durability of bricks used in the conservation of historic buildings — influence of composition and microstructure, Journal of Cultural Heritage 4 (2) (2003) 91–99, https://doi.org/10.1016/S1296-2074(03)00020-7. ISSN 1296-2074. URL https://www.sciencedirect.com/science/article/pii/S1296207403000207.
[22] A. Erker, The thermal conductivity of the brick ceramic body (part 2), Ziegelindustrie International 55 (2002) 32–37.
[23] J.D. Eshelby, The determination of the elastic field of an ellipsoidal inclusion, and related problems, Proc. R. Soc. London Ser. A 241 (1226) (1957) 376–396.
[24] J. Füssl, M. Li, M. Lukacevic, J. Eberhardsteiner, C. Martin, Comparison of unit cell-based computational methods for predicting the strength of wood, Eng. Struct. 141 (2017) 427–443, https://doi.org/10.1016/j.engstruct.2017.03.005. ISSN 0141-0296. URL https://www.sciencedirect.com/science/article/pii/S0141029617307253.
[25] J. García-Ten, M. Orts, A. Saburit, G. Silva, Thermal conductivity of traditional ceramics. Part I: Influence of bulk density and firing temperature, Ceram. Int. 36 (2010) 1951–1959, https://doi.org/10.1016/j.ceramint.2010.05.012. URL https://doi.org/10.1016/j.ceramint.2010.05.012.
[26] J. García-Ten, M. Orts, A. Saburit, G. Silva, Thermal conductivity of traditional ceramics Part II: Influence of mineralogical composition, Ceram. Int. 36 (2010) 2017–2024, https://doi.org/10.1016/j.ceramint.2010.05.013. URL https://doi.org/10.1016/j.ceramint.2010.05.013.
[27] A. Giraud, C. Gruescu, D. Do, F. Homand, D. Kondo, Effective thermal conductivity of transversely isotropic mediawith arbitrary oriented ellipsoidal inhomogeneities, Int. J. Solids Struct. 44 (2007) 2627–2647, https://doi.org/10.1016/j.ijsolstr.2006.08.011. URL https://doi.org/10.1016/j.ijsolstr.2006.08.011.
[28] S. Grandjean, J. Absi, and D. Smith. Numerical calculations of the thermal conductivity of porous ceramics based on micrographs. Journal of the European Ceramic Society, 26 (13): 2669–2676, 2006. ISSN 0955–2219. doi: 10.1016/j.jeurceramsoc.2005.07.061. http://www.sciencedirect.com/science/article/pii/S0955221905007478.
[29] M.L. Gualtieri, A.F. Gualtieri, S. Gagliardi, P. Ruffini, R. Ferrari, M. Hanuskova, Thermal conductivity of fired clays: Effects of mineralogical and physical properties of the raw materials, Appl. Clay Sci. 49 (2010) 269–275, https://doi.org/10.1016/j.clay.2010.06.002. URL https://doi.org/10.1016/j.clay.2010.06.002s.
[30] A. Hein, N.S. Müller, P.M. Day, V. Kilikoglou, Thermal conductivity of archaeological ceramics: The effect of inclusions, porosity and firing temperature, Thermochim. Acta (2008), https://doi.org/10.1016/j.tca.2008.09.012. URL https://doi.org/10.1016/j.tca.2008.09.012.
[31] R. Hill, Elastic properties of reinforced solids: some theoretical principles, J. Mech. Phys. Solids 11 (1963) 357–372, https://doi.org/10.1016/0022-5096(63)90036-X. URL https://www.doi.org/10.1016/0022-5096(63)90036-X.
[32] R. Hill, Continuum micro-mechanics of elastoplastic polycrystals, J. Mech. Phys. Solids 13 (2) (1965) 89–101, https://doi.org/10.1016/0022-5096(65)90023-2. URL https://doi.org/10.1016/0022-5096(65)90023-2.
[33] S. Hríbalová, T. Uhlírová, W. Pabst, Computer modeling of systematic processing defects on the thermal and elastic properties of open kelvin-cell metamaterials, J. Eur. Ceram. Soc. 41 (14) (2021) 7130–7140, https://doi.org/10.1016/j.jeurceramsoc.2021.07.031. ISSN 0955-2219. URL https://www.sciencedirect.com/science/article/pii/S095522192100501X.
[34] H. Kariem, C. Hellmich, T. Kiefer, A. Jäger, J. Füssl, Micro-CT-based identification of double porosity in fired clay ceramics, J. Mater. Sci. 53 (13) (2018) 9411–9428, https://doi.org/10.1007/s10853-018-2281-9. ISSN 1573-4803. doi: 10.1007/s10853-018-2281-9. URL https://doi.org/10.1007/s10853-018-2281-9.
[35] H. Kariem, J. Füssl, T. Kiefer, A. Jäger, C. Hellmich, The viscoelastic behaviour of material phases in fired clay identified by means of grid nanoindentation, Constr. Build. Mater. 231 (2020) 117066, https://doi.org/10.1016/j.conbuildmat.2019.117066. ISSN 0950-0618. URL http://www.sciencedirect.com/science/article/pii/S0950061819325085.
[36] H. Kariem, T. Kiefer, C. Hellmich, W. Gaggl, A. Steiger-Thirsfeld, J. Füssl, Edx/xrd-based identification of micrometer-sized domains in scanning electron micrographs of fired clay, Mater. Struct. 53 (109) (2020), https://doi.org/10.1617/s11527-020-01531-7. URL https://doi.org/10.1617/s11527-020-01531-7.
[37] T. Kiefer, H. Kariem, M. Lukacevic, J. Füssl, The compressive strength of vertically perforated clay block masonry predicted by means of a unit-cell type numerical simulation tool taking discrete cracking into account, Constr. Build. Mater. 150 (2017) 24–34, https://doi.org/10.1016/j.conbuildmat.2017.05.201. ISSN 0950-0618. URL https://www.sciencedirect.com/science/article/pii/S0950061817310991.
[38] T. Kiefer, J. Füssl, H. Kariem, J. Konnerth, W. Gaggl, C. Hellmich, A multi-scale material model for the estimation of the transversely isotropic thermal conductivity tensor of fired clay bricks, J. Eur. Ceram. Soc. 40 (15) (2020) 6200–6217, https://doi.org/10.1016/j.jeurceramsoc.2020.05.018. ISSN 0955-2219. URL https://www.sciencedirect.com/science/article/pii/S0955221920303691.
[39] V. Kilikoglou, G. Vekinis, Y. Maniatis, Toughening of ceramic earthenwares by quartz inclusions: An ancient art revisited, Acta Metall. Mater. 43 (8) (1995) 2959–2965, https://doi.org/10.1016/0956-7151(95)00006-H. URL https://doi.org/10.1016/0956-7151(95)00006-H.
[40] V. Kilikoglou, G. Vekinis, Y. Maniatis, P.M. Day, Mechanical performance of quartz-tempered ceramics: Part I, strength and toughness, Archoeornetry 40 (2) (1998) 261–279, https://doi.org/10.1111/j.1475-4754.1998.tb00837.x. URL https://doi.org/10.1111/j.1475-4754.1998.tb00837.x.
[41] C. Kohlhauser, C. Hellmich, Ultrasonic contact pulse transmission for elastic wave velocity and stiffness determination: Influence of specimen geometry and porosity, Eng. Struct. 47 (2013) 115–133, https://doi.org/10.1016/j.engstruct.2012.10.027. URL https://doi.org/10.1016/j.engstruct.2012.10.027.
[42] M. Königsberger, B. Pichler, C. Hellmich, Multiscale poro-elasticity of densifying calcium-silicate hydrates in cement paste: An experimentally validated continuum micromechanics approach, Int. J. Eng. Sci. 147 (2020), https://doi.org/10.1016/j.ijengsci.2019.103196. ISSN 00207225. URL https://doi.org/10.1016/j.ijengsci.2019.103196.
[43] K.J. Krakowiak, P.B. Lourenço, F.J. Ulm, Multitechnique investigation of Extruded Clay Brick Microstructure, J. Am. Ceram. Soc. 94 (9) (2011) 3012–3022, https://doi.org/10.1111/j.1551-2916.2011.04484.x. URL https://doi.org/10.1111/j.1551-2916.2011.04484.x.
[44] M. Kubis, K. Pietrak, Lukasz Cieslikiewicz, P. Furmanski, M. Wasik, M. Seredynski, T.S. Wisniewski, P. Lapka, On the anisotropy of thermal conductivity in ceramic bricks, Journal of Building Engineering 31 (2020) 101418, https://doi.org/10.1016/j.jobe.2020.101418. ISSN 2352-7102. URL https://www.sciencedirect.com/science/article/pii/S2352710219325719.
[45] C. Liu, R. Qian, Z. Liu, G. Liu, Y. Zhang, Multi-scale modelling of thermal conductivity of phase change material/recycled cement paste incorporated cement-based composite material, Materials & Design 191 (2020) 108646, https://doi.org/10.1016/j.matdes.2020.108646. ISSN 0264-1275. URL https://www.sciencedirect.com/science/article/pii/S0264127520301805.
[46] P. Maillard, J. Aubert, Effects of the anisotropy of extruded earth bricks on their hygrothermal properties, Constr. Build. Mater. 63 (2014) 56–61, https://doi.org/10.1016/j.conbuildmat.2014.04.001. ISSN 0950-0618. URL https://www.sciencedirect.com/science/article/pii/S0950061814003183.
[47] T. Mori, K. Tanaka, Average stress in matrix and average elastic energy of materials with misfitting inclusions, Acta Metall. 21 (5) (1973) 571–574,

https://doi.org/10.1016/0001-6160. ISSN 0001-6160. URL https://www.sciencedirect.com/science/article/pii/0001616073900643.
[48] N.S. Müller, V. Kilikoglou, P.M. Day, G. Vekinis, The influence of temper shape on the mechanical properties of archaeological ceramics, J. Eur. Ceram. Soc. 30 (2010) 2457–2465, https://doi.org/10.1016/j.jeurceramsoc.2010.04.039. URL https://doi.org/10.1016/j.jeurceramsoc.2010.04.039.
[49] N.S. Müller, G. Vekinis, P. Day, V. Kilikoglou, The influence of microstructure and texture on the mechanical properties of rock tempered archaeological ceramics, J. Eur. Ceram. Soc. 35 (2015) 831–843, https://doi.org/10.1016/j.jeurceramsoc.2014.09.025. URL https://doi.org/10.1016/j.jeurceramsoc.2014.09.025.
[50] T. Mura, Micromechanics of defects in solids, volume 3, Springer, 1987.
[51] T. Nguyen, F. Meftah, Behavior of hollow clay brick masonry walls during fire part 2: 3d finite element modeling and spalling assessment, Fire Saf. J. 66 (2014) 35–45, https://doi.org/10.1016/j.firesaf.2013.08.017. ISSN 0379-7112. URL https://www.sciencedirect.com/science/article/pii/S037971121300180X.
[52] T. Ohmura, M. Tsuboi, T. Tomimura, Estimation of the Mean Thermal Conductivity of Anisotropic Materials, Int. J. Thermophys. 23 (2002) 843–853, https://doi.org/10.1023/A:1015423708823. URL https://doi.org/10.1023/A:1015423708823.
[53] W. Pabst, E. Gregorová, A cross-property relation between the tensile modulus and the thermal conductivity of porous materials, Ceram. Int. 33 (2007) 9–12, https://doi.org/10.1016/j.ceramint.2005.07.009. URL https://doi.org/10.1016/j.ceramint.2005.07.009.
[54] W. Pabst, E. Gregorová, A generalized cross-property realtion between the elastic moduli and conductivity of isotropic porous materials with spheroidal pores, Ceramics-Silikáty 61 (1) (2017) 74–80, https://doi.org/10.13168/cs.2016.0063. URL https://doi.org/10.13168/cs.2016.0063.
[55] W. Pabst and T. Uhlířová. Benchmark polynomials for the porosity dependence of elastic moduli and conductivity of partially sintered ceramics. Journal of the European Ceramic Society, 2021. ISSN 0955-2219. doi: https://doi.org/10.1016/j.jeurceramsoc.2021.08.028. URL https://www.sciencedirect.com/science/article/pii/S0955221921005951.
[56] B. Pichler, C. Hellmich, Upscaling quasi-brittle strength of cement paste and mortar: A multi-scale engineering mechanics model, Cem. Concr. Res. 41 (5) (2011) 467–476, https://doi.org/10.1016/j.cemconres.2011.01.010.
[57] C. Pichler, R. Traxl, R. Lackner, Power-law scaling of thermal conductivity of highly porous ceramics, J. Eur. Ceram. Soc. 35 (6) (2015) 1933–1941, https://doi.org/10.1016/j.jeurceramsoc.2014.12.004. ISSN 0955-2219. URL http://www.sciencedirect.com/science/article/pii/S095522191400661X.
[58] E. Segnit, C. Anderson, Scanning electron microscopy of fired illite, Transactions and Journal of the British Ceramics Society 71 (1972) 85–88. URL http://hdl.handle.net/102.100.100/314482?index=1.
[59] I. Sevostianov, M. Kachanov, On some controversial issues in effective field approaches to the problem of the overall elastic properties, Mech. Mater. 69 (1) (2014) 93–105, https://doi.org/10.1016/j.mechmat.2013.09.010. ISSN 0167-6636. URL https://www.sciencedirect.com/science/article/pii/S0167663613001853.
[60] R. Snellings, Ö. Cizer, L. Horckmans, P. Durdziński, P. Dierckx, P. Nielsen, K.V. Balen, L. Vandewalle, Properties and pozzolanic reactivity of flash calcined dredging sediments, Appl. Clay Sci. 129 (2016) 35–39, https://doi.org/10.1016/j.clay.2016.04.019. ISSN 0169-1317. URL https://www.sciencedirect.com/science/article/pii/S0169131716301806.
[61] R. Suda, T. Kiefer, C. Schranz, J. Füssl, A finite-element-based approach to quantify the impact of bed joint reinforcement on the compressive strength of vertically perforated clay block masonry, Eng. Struct. 239 (2021) 112277, https://doi.org/10.1016/j.engstruct.2021.112277. ISSN 0141-0296. URL https://www.sciencedirect.com/science/article/pii/S0141029621004272.
[62] M. Tite, Y. Maniatis, Examination of ancient pottery using the scanning electron microscope, Nature 257 (1975) 122–123, https://doi.org/10.1038/257122a0. URL https://doi.org/10.1038/257122a0.
[63] M.S. Tite, V. Kilikoglou, G. Vekinis, Strength, toughness and thermal shock resistance of ancient ceramics, and their influence on techno- logical choice, Archaeometry 43 (3) (2001) 301–324, https://doi.org/10.1111/1475-4754.00019. URL https://doi.org/10.1111/1475-4754.00019.
[64] T. Uhlířová, V. Necina, W. Pabst, Modeling of young's modulus and thermal conductivity evolution of partially sintered alumina ceramics with pore shape changes from concave to convex, J. Eur. Ceram. Soc. 38 (8) (2018) 3004–3011, https://doi.org/10.1016/j.jeurceramsoc.2017.12.033. ISSN 0955-2219. URL https://www.sciencedirect.com/science/article/pii/S0955221917308439. Cermodel 2017: Modelling and Simulation Meet Innovation in Ceramics Technology.
[65] F.-J. Ulm, A. Delafargue, and G. Constantinides. Applied Micromechanics of Porous Materials, CSIM Courses and Lectures No. 480. Springer Wien New York, 2005.
[66] M. Šveda, Influence of calcium carbonate on the physical properties of a clay body. part 1. Ziegelindustrie, International 53 (2000) 40–46.
[67] H. Wang, X. Liu, H. Zhang, P. Apostolidis, S. Erkens, A. Skarpas, Micromechanical modelling of complex shear modulus of crumb rubber modified bitumen, Materials & Design 188 (2020) 108467, https://doi.org/10.1016/j.matdes.2019.108467. ISSN 0264-1275. URL https://www.sciencedirect.com/science/article/pii/S0264127519309050.
[68] A. Zaoui, Continuum Micromechanics: Survey, Journal of Engineering Mechanics 128 (2) (2002) 808–816, https://doi.org/10.1061/(asce)0733-9399(2002)128:8(808). URL https://doi.org/10.1061/(asce)0733-9399(2002)128:8(808).
[69] H. Zhang, K. Anupam, T. Scarpas, C. Kasbergen, S. Erkens, Contact mechanics based solution to predict modulus of asphalt materials with high porosities, Materials & Design 206 (2021) 109752, https://doi.org/10.1016/j.matdes.2021.109752. ISSN 0264-1275. URL https://www.sciencedirect.com/science/article/pii/S0264127521003051.
[70] F. Zunino, E. Boehm-Courjault, K. Scrivener, The impact of calcite impurities in clays containing kaolinite on their reactivity in cement after calcination, Mater. Struct. 53 (2020) 44, https://doi.org/10.1617/s11527-020-01478-9. URL https://doi.org/10.1617/s11527-020-01478-9.
[71] Z. Živcová, E. Gregorová, W. Pabst, D.S. Smith, A. Michot, C. Poulier, Thermal conductivity of porous alumina ceramics prepared using starch as a pore-forming agent, J. Eur. Ceram. Soc. 29 (3) (2009) 347–353, https://doi.org/10.1016/j.jeurceramsoc.2008.06.018. ISSN 0955-2219. URL http://www.sciencedirect.com/science/article/pii/S0955221908003233.
[72] Z. Živcová, M. Cerný, W. Pabst, E. Gregorová, Elastic properties of porous oxide ceramics prepared using starch as a pore-forming agent, J. Eur. Ceram. Soc. 29 (13) (2009) 2765–2771, https://doi.org/10.1016/j.jeurceramsoc.2009.03.033. ISSN 0955-2219, URL http://www.sciencedirect.com/science/article/pii/S0955221909001496.